Physics – Uspekhi **55** (2) 115 – 136 (2012)

REVIEWS OF TOPICAL PROBLEMS PACS numbers: **52.30.–q**, 97.10.Gz, **97.80.–d**

Flow structure in magnetic close binary stars

A G Zhilkin, D V Bisikalo, A A Boyarchuk

DOI: 10.3367/UFNe.0182.201202a.0121

Contents

Abstract. **The current understanding of mass exchange processes between close binary system (CBS) components is reviewed, with particular attention on the mass flow structure and accretion disk physics. Using 3D MHD calculation results, the variation of key accretion disk characteristics with the accretor magnetic field is studied and the magnetic field generation process is analyzed. In particular, it is shown that the quasi-periodic process of toroidal magnetic field generation in disks results in alternating accretion and decretion regimes in the inner regions of the disk. By treating MHD flows in CBSs self-consistently, disk formation conditions are established and a separation criterion between intermediate-polar and polar flows is found. The possibility of using MHD simulation results for explaining observations is discussed.**

A G Zhilkin Institute of Astronomy, Russian Academy of Sciences, ul. Pyatnitskaya 48, 119017 Moscow, Russian Federation
Tel. +7 (495) 951 79 93. Fax +7 (495) 230 20 81
E-mail: zhilkin@inasan.ru
Chelyabinsk State University, ul. Bratiev Kashirinykh 129, 454001 Chelyabinsk, Russian Federation
Tel. +7 (351) 799 71 93. Fax +7 (351) 741 97 67
D V Bisikalo, A A Boyarchuk Institute of Astronomy, Russian Academy of Sciences, ul. Pyatnitskaya 48, 119017 Moscow, Russian Federation
E-mail: bisikalo@inasan.ru, aboyar@inasan.ru

Received 17 May 2011, revised 14 July 2011
Uspekhi Fizicheskikh Nauk **182** (2) 121 – 145 (2012)
DOI: 10.3367/UFNr.0182.201202a.0121
Translated by K A Postnov; edited by A M Semikhatov

1. Introduction

According to modern evolutionary models, about 80% of all stars are born in binaries (see, e.g., [1]). In a binary system, a more massive (primary) star evolves faster than the less massive (secondary) component and eventually forms a compact object, which can be a white dwarf, a neutron star, or a black hole, depending on the initial mass of the star. If the radius of the secondary component during evolutionary expansion reaches the libration point (the so-called inner Lagrange point L_1) where all forces except the pressure gradient are balanced, the matter of the secondary star starts falling (accreting) onto the compact object. Such binary stars are called close binary systems (CBSs). The gas dynamics of matter flow from the vicinity of the L_1 point have been studied by many authors. This problem was first analyzed semi-analytically in [2, 3], and its modern treatment is reviewed in [4–6]. Presently, it is recognized that the gas dynamics of gas flows in a nonmagnetic semi-detached CBS are determined by the formation of a gas stream from L_1, a quasi-elliptic accretion disc, a disc halo, and a circumbinary shell [4]. The classification of the main elements of the gas flow in such binaries introduced in [4] is based on their physical properties: (1) if the gas flow is not determined by the gravity field of the accretor, a circumbinary envelope filling the space between the binary components is formed; (2) if the gas rotates around the accretor and is then mixed with stream matter, it does not belong to the disc and forms a circumdisc halo; (3) an accretion disc is formed by the stream; the disc matter does not interact with the stream any more and moves toward the compact object, losing its angular momentum.

There are many CBSs in which the magnetic field plays a substantial role in the mass transfer and accretion processes.

These are, first of all, magnetic cataclysmic variables and X-ray binaries. In magnetic cataclysmic variables, accretion proceeds onto a magnetic white dwarf with the surface magnetic field $\sim 10^4 - 10^8$ G. In X-ray binaries, accretion occurs onto a neutron star with the magnetic field $\sim 10^{12}$–10^{13} G. Simple estimates show that the dipole magnetic moments of white dwarfs in magnetic cataclysmic variables and neutron stars in X-ray binaries are of the same order of magnitude: about 10^{30} G cm^3. This implies that magnetosphere radii $r_{\rm m}$ of a white dwarf and a neutron star are approximately the same [see formula (33)]. This radius determines the degree of influence of the magnetic field on the flow structure in CBSs. However, in cataclysmic variables, the distance between the components A can be tens and hundreds of times smaller than in X-ray binaries. Therefore, the dimensionless magnetosphere radius $r_{\rm m}/A$ in magnetic cataclysmic variables can be much larger than that in X-ray binaries. Hence, the effect of the accretor magnetic field on the mass transfer process and the structure of the accretion disc in cataclysmic variables can be much stronger than in X-ray binaries. Because we are primarily interested in the outer parts of the accretion disc, which are observed in classical astronomy, we focus on the flow structure in magnetic cataclysmic variables.

In magnetic cataclysmic variables, the matter from the donor star (which is a low-mass late-type dwarf) is transferred through the inner Lagrange point onto a white dwarf (see, e.g., [5]). Two main types of magnetic cataclysmic variables can be distinguished: polars and intermediate polars. In polars (AM Her-type stars), the white dwarf has a strong surface magnetic field $\sim 10^7 - 10^8$ G. Observations show that polars are characterized by relatively short orbital periods of 1 to 5 hours. Accretion discs in such systems are not observed, and the components are rotating synchronously [7]. So-called magnetors [8], in which the inner Lagrange point lies inside the accretor magnetosphere, represent the limiting case. In polars, the gas from the donor star is believed to form a collimated flow canalized by magnetic field lines, which accretes onto one of the magnetic poles of the accretor [5, 9].

Intermediate polars are CBSs with relatively weak surface magnetic fields ($\sim 10^4 - 10^6$ G) of the accreting white dwarf. They occupy an intermediate position between polars and nonmagnetic cataclysmic variables. Intermediate polars have orbital periods in a wide range from several hours to several dozen hours. The spin period of accretors in these systems is significantly shorter than orbital periods (by tens, hundreds, and even thousands of times) [7]. In the DQ Her subclass of intermediate polars, the difference in the white dwarf spin and orbital periods is more pronounced. Depending on the spin-to-orbital period ratio, other systems are divided into regular intermediate polars, EX Hya systems, and systems with almost synchronous rotation [7]. The asynchronous spin rotation of the accretor in intermediate polars is explained by the interaction of the white dwarf magnetic field with disc matter in the magnetospheric boundary region, which results in the equilibrium rotation period when the corotation radius is equal to the magnetosphere radius [5, 9].

Studies of MHD flows in binary systems are complicated because even in the simplified case, the flow can be essentially three-dimensional. However, this problem is very interesting, because all observed phenomena in close binary stars in one way or another are related to the accretion of matter onto one of the components. Accretion onto a magnetized compact object can lead to observational phenomena, including the radiation from polar columns, variability due to the formation of a hot spot on the accretor surface, high-frequency quasiperiodic oscillations of X-ray emission, etc.

Of special importance is the correct treatment of MHD processes in accretion discs in CBSs: in semidetached binaries, the magnetic field is initially not sufficiently strong in the accretion disc formation region. But the magnetic field of the accretor can be amplified in the accretion disc due to differential rotation, radial motions, and the dynamo mechanism. Diffusion, turbulent dissipation, and magnetic buoyancy decrease the magnetic field. As the result of all these processes, the magnetic field configuration becomes intricate, because different effects can dominate in different parts of the disc. We note that in contrast to single stars (a star, an accretion disc, etc.), specific mechanisms of magnetic field generation can operate in close binaries [10]. In polars, for example, the Herzenberg dynamo can work [11, 12], which leads to the magnetic field generation in the envelope of the secondary. The presence of a magnetic field in the disc essentially determines the disc properties; hence, its study is important for the interpretation of observations. Moreover, magnetic fields in the disc can lead to the formation of bipolar outflows [13]. Finally, the magnetic field can play a role in the generation of turbulence in the disc via magneto-rotational instability [14, 15].

Three-dimensional numerical modeling of mass transfer in semi-detached binary systems without a magnetic field was carried out in [4, 16–19]. In these papers, a self-consistent gasdynamic model of gas flows in CBSs was developed for the first time and characteristics of the main features of the flow structure were obtained. Attempts at numerical studies of magnetic field effects on the flow structure have been made since the 1990s. But due to the complexity of the problem, the studies were carried out either using oversimplified models or in the restricted region of the star magnetosphere. Even simplified quasiparticle modeling [7, 20–25] showed that in intermediate polars, depending on the system parameters, flows of very different structures can form: from accretion flows canalized by the magnetic field to accretion discs, as in nonmagnetic cataclysmic variables. However, these models ignored important effects, including gas and magnetic pressure and the cooling and heating of matter, and therefore the results of those calculations can be applied only to a qualitative analysis and cannot be used for the interpretation of observational data. Accretion inside the star magnetosphere has been studied more thoroughly. For example, papers [26–29] describe the results of three-dimensional modeling of plasma accretion onto a gravitating object with a dipole magnetic field whose axis is tilted to the spin axis of the star. These calculations allowed the three-dimensional structure of the flow inside the accretor magnetosphere, where the magnetic field dominates, to be studied in detail.

Only recently have the authors of this review managed to develop a complete three-dimensional numerical model for calculation of the gas flow structure in close binaries [30–33]. In our approach, the complete system of MHD equations is used, which allows describing all the principal dynamic effects related to the magnetic field. The numerical model takes radiation cooling and heating into account, together with magnetic field diffusion due to current dissipation in turbulent eddies, magnetic buoyancy, and wave MHD turbulence. It is important to note that the formation and subsequent evolution of an accretion disc occurs naturally in our model due to the mass transfer via the inner Lagrange

point. Thus, for the first time we are able to self-consistently describe the structure of MHD flows in close binaries and to obtain results that can be used for interpretation of real astronomical observations.

2. The model

2.1 The problem setting

In semidetached close binaries, the donor star fills its internal critical surface, which can be identified with the Roche lobe in a restricted three-body problem. In the reference frame rotating with the orbital angular velocity $\mathbf{\Omega}$ of the binary system around the barycenter, the Roche potential has the form

$$\Phi = -\frac{GM_{\mathrm{a}}}{|\mathbf{r}-\mathbf{r}_{\mathrm{a}}|} - \frac{GM_{\mathrm{d}}}{|\mathbf{r}-\mathbf{r}_{\mathrm{d}}|} - \frac{1}{2}\left[\mathbf{\Omega}\times(\mathbf{r}-\mathbf{r}_{\mathrm{c}})\right]^2 , \tag{1}$$

where G is the Newton gravity constant, M_{a} and M_{d} are the accretor and donor masses, and radius vectors $\mathbf{r}_{\mathrm{a}}$, $\mathbf{r}_{\mathrm{d}}$, and $\mathbf{r}_{\mathrm{c}}$ determine the position of the centers of the accretor, donor, and system barycenter. The mass exchange in the system occurs through the inner Lagrange point L_1, since the pressure gradient is not counterbalanced by the gravity force at that point.

To describe the flow in a binary system, we use the Cartesian system (x, y, z) specified as follows. The origin is at the accretor center: $\mathbf{r}_{\mathrm{a}} = (0, 0, 0)$. The donor center lies at a distance A on the x axis from the accretor center, $\mathbf{r}_{\mathrm{d}} = (-A, 0, 0)$. The z axis is directed along the orbital rotation axis $\mathbf{\Omega} = (0, 0, \Omega)$.

Typically, magnetic fields of white dwarfs in intermediate polars can be well described by a dipole field. However, magnetic cataclysmic variables include systems in which the white dwarf has a complex magnetic field [34, 35]. Such a field can be represented by a superposition of multipole field components. The character of accretion onto the white dwarf with a complex magnetic field can differ significantly from the pure dipole case. In particular, such a field configuration can have several poles onto which accretion is possible.

In the absence of currents in the binary system envelope, the magnetic field is entirely determined by the proper field of the accretor $\mathbf{B}_*$. Because this field is determined by currents distributed inside the accretor, it must be potential, $\mathrm{rot}\,\mathbf{B}_* = 0$, and can therefore be described by a scalar potential, $\mathbf{B}_* = -\mathrm{grad}\,\varphi$. In what follows, we assume each multipole component of the field to be axially symmetric. Symmetry axes of different multipole components can be different in general. In our model, only dipole and quadrupole components of the accretor magnetic field are taken into account.

The potential corresponding to the dipole field component is given by [36]

$$\varphi_{\mathrm{d}} = \frac{\mu(\mathbf{dr})}{r^3} , \tag{2}$$

where μ is the magnetic moment of the accretor and $\mathbf{d}$ is the unit vector determining the dipole symmetry axis. The magnetic moment vector is $\boldsymbol{\mu} = \mu\mathbf{d}$. The magnetic field induction is

$$\mathbf{B}_{\mathrm{d}} = \frac{\mu}{r^3}\left[3(\mathbf{dn})\mathbf{n} - \mathbf{d}\right] , \tag{3}$$

where $\mathbf{n} = \mathbf{r}/r$. We let $B_{\mathrm{d,a}}$ denote the magnetic field strength at the dipole magnetic pole. From (3), we then obtain the magnetic moment $\mu = B_{\mathrm{d,a}} R_{\mathrm{a}}^3/2$, where R_{a} is the accretor radius.

The potential corresponding to the quadrupole field component [36] is given by

$$\varphi_{\mathrm{q}} = D_{ik}\,\frac{n_i n_k}{2r^3} , \tag{4}$$

where D_{ik} is the quadrupole moment tensor of the accretor. If the current distribution in the accretor is axially symmetric, diagonal components of the quadrupole moment relative to the symmetry axis are $D_{11} = D_{22} = -D/2$, and $D_3 = D$, while nondiagonal components vanish. In this case, the potential of the quadrupole magnetic field is

$$\varphi_{\mathrm{q}} = \frac{D}{4r^3}\left[3(\mathbf{qn})^2 - 1\right] , \tag{5}$$

where $\mathbf{q}$ is the unit vector determining the symmetry axis of the quadrupole. The corresponding magnetic field induction is

$$\mathbf{B}_{\mathrm{q}} = \frac{3D}{4r^4}\left[5(\mathbf{qn})^2\mathbf{n} - \mathbf{n} - 2(\mathbf{qn})\mathbf{q}\right] . \tag{6}$$

We now let $B_{\mathrm{q,a}}$ denote the quadrupole magnetic field at the quadrupole pole. From Eqn (6), we then obtain the quadrupole magnetic moment $D = 2B_{\mathrm{q,a}} R_{\mathrm{a}}^4/3$.

The total magnetic field of the accretor in our model is $\mathbf{B}_* = \mathbf{B}_{\mathrm{d}} + \mathbf{B}_{\mathrm{q}}$. Simple analysis of Eqns (3) and (6) shows that for $B_{\mathrm{q,a}} > B_{\mathrm{d,a}}$, a region near the accretor exists where the quadrupole field dominates over the dipole one. In the opposite case, $B_{\mathrm{q,a}} < B_{\mathrm{d,a}}$, the plasma flow near the accretor is fully controlled by the dipole magnetic field.

In the general case, the spin of the accretor is asynchronous and is characterized in the chosen reference frame by an angular velocity $\mathbf{\Omega}_*$. In our model, we consider the case where the spin axis of the accretor coincides with the orbital rotation axis. On the other hand, vectors $\mathbf{d}$ and $\mathbf{q}$ determining the dipole and quadrupole magnetic field moments cannot coincide with the direction of the orbital angular velocity vector $\mathbf{\Omega}$. Let the vector $\mathbf{d}$ be inclined to the axis z by an angle θ_{d}, and the time-dependent angle between the projection of $\mathbf{d}$ onto the xy plane be $\phi_{\mathrm{d}} = \Omega_* t + \phi_{\mathrm{d0}}$, where ϕ_{d0} is the initial value of this angle. Similar angles θ_{q} and ϕ_{q} can be introduced for the vector $\mathbf{q}$. The magnetic field of the accretor is then time dependent:

$$\frac{\partial \mathbf{B}_*}{\partial t} = \mathrm{rot}\,(\mathbf{v}_* \times \mathbf{B}_*) , \tag{7}$$

where $\mathbf{v}_* = \mathbf{\Omega}_* \times (\mathbf{r} - \mathbf{r}_{\mathrm{a}})$ is the velocity of the accretor magnetic lines. We note that when $\Omega_* = 0$ (synchronous rotation of the accretor) and $\theta_{\mathrm{d,q}} = 0, \pi$ (the accretor magnetic axis is aligned with its spin axis), the magnetic field of the accretor is stationary.

2.2 Plasma in a strong magnetic field

Simple estimates show that in accretion streams of polars, the propagation velocity of Alfvén and magnetosonic waves can be much higher than the bulk velocity of plasma, and can in some cases be relativistic. Therefore, the use of nonrelativistic magneto gas dynamics to model the structure of such a flow, strictly speaking, is incorrect. A more correct treatment could be achieved in the framework of relativistic magneto gas

dynamics. However, in our case, the flow can be described using a simpler model. Indeed, the gas stream in CBSs is essentially nonrelativistic; only Alfvén and magnetosonic waves propagate with relativistic velocities. In the characteristic dynamic evolution time of slow plasma motion, the MHD waves pass along and across the stream many times. As a result, the plasma dynamics in the stream can be considered in the framework of the modified nonrelativistic magneto gas dynamics as some averaged flow on the background of a specific wave MHD turbulence.

Thus, plasma dynamics in a strong external magnetic field are characterized by a relatively slow mean motion of particles along the magnetic field, a drift across the magnetic field lines, and a very high velocity propagation of Alfvénic and magnetosonic waves on top of them. To describe the structure of such a flow, we can use the averaged picture by considering the effect of rapid pulsations, similarly to the treatment of the wave MHD turbulence. To describe the slow motion of plasma, it is necessary to single out rapidly propagating fluctuations and to average in a certain way over the ensemble of wave pulsations.

We consider the relation

$$\mathbf{E} + \frac{(\mathbf{v} \times \mathbf{B})}{c} = \frac{\mathbf{j}}{\sigma}\,, \tag{8}$$

which expresses Ohm's law for a plasma in magneto gas dynamics [37]. Here, $\mathbf{E}$ is the electric field strength in the plasma, $\mathbf{B} = \mathbf{B}_* + \mathbf{b}$ is the total magnetic field induction including the magnetic field of the accretor $\mathbf{B}_*$ and the proper plasma field $\mathbf{b}$, $\mathbf{j}$ is the current density, and σ is the electric conductivity. We represent dynamic variables as the sum of the mean value and fluctuations, for example, $\mathbf{b} = \langle\mathbf{b}\rangle + \delta\mathbf{b}$. Averaging Eqn (8), we then find

$$c\langle\mathbf{E}\rangle + \langle\mathbf{v}\rangle \times \langle\mathbf{b}\rangle + \langle\mathbf{v}\rangle \times \mathbf{B}_* + \langle\delta\mathbf{v} \times \delta\mathbf{b}\rangle = \frac{c\langle\mathbf{j}\rangle}{\sigma}\,. \tag{9}$$

The last term in the left-hand side can be estimated using the well-known expression in the dynamo theory (see, e.g., [38, 39])

$$\langle\delta\mathbf{v} \times \delta\mathbf{b}\rangle = \alpha\langle\mathbf{b}\rangle - \eta_{\mathrm{w}}\,\mathrm{rot}\,\langle\mathbf{b}\rangle\,, \tag{10}$$

where α is determined by the mean helicity of the flow and η_{w} is the diffusion coefficient of the mean magnetic field caused by the wave MHD turbulence. The first term (the α-effect) can be neglected because it describes a relatively weak and slow process of generation of the mean magnetic field in the accretion disc.

Averaging the Maxwell equation

$$\mathrm{rot}\,\mathbf{B} = \frac{4\pi}{c}\,\mathbf{j}\,, \tag{11}$$

we find

$$\langle\mathbf{j}\rangle = \frac{c}{4\pi}\,\mathrm{rot}\,\langle\mathbf{b}\rangle\,. \tag{12}$$

Substituting Eqns (10) and (12) in (9), we obtain

$$c\langle\mathbf{E}\rangle + \langle\mathbf{v}\rangle \times \langle\mathbf{b}\rangle + \langle\mathbf{v}\rangle \times \mathbf{B}_* - \eta_{\mathrm{w}}\,\mathrm{rot}\,\langle\mathbf{b}\rangle = \eta_{\mathrm{OD}}\,\mathrm{rot}\,\langle\mathbf{b}\rangle\,, \tag{13}$$

where $\eta_{\mathrm{OD}} = c^2/(4\pi\sigma)$ is the coefficient of the Ohmic diffusion of the magnetic field. Typically, $\eta_{\mathrm{w}} \gg \eta_{\mathrm{OD}}$, and hence the right-hand side can be neglected. In addition, in strong external magnetic fields, the second term is much smaller than the third one. Then, averaging the Maxwell electromagnetic induction equation,

$$\mathrm{rot}\,\mathbf{E} = -\frac{1}{c}\frac{\partial\mathbf{B}}{\partial t}\,, \tag{14}$$

we obtain

$$c\,\mathrm{rot}\,\langle\mathbf{E}\rangle = -\frac{\partial\langle\mathbf{b}\rangle}{\partial t} - \mathrm{rot}\,(\mathbf{v}_* \times \mathbf{B}_*)\,. \tag{15}$$

The first term in the right-hand side is due to the change in the mean magnetic field $\langle\mathbf{b}\rangle$ over the characteristic dynamic time. This term is of the order of the second term in Eqn (13). Therefore, the mean electric field strength can be estimated from the expression

$$c\langle\mathbf{E}\rangle = -\mathbf{v}_* \times \mathbf{B}_*\,. \tag{16}$$

Keeping leading-order terms in (13), we arrive at

$$\eta_{\mathrm{w}}\,\mathrm{rot}\,\langle\mathbf{b}\rangle = \big(\langle\mathbf{v}\rangle - \mathbf{v}_*\big) \times \mathbf{B}_*\,. \tag{17}$$

The obtained formula can be used to calculate the mean electromagnetic field in the equation of motion. Neglecting density fluctuations and wave magnetic pressure and tension, we find

$$\frac{\langle\mathbf{B} \times \mathrm{rot}\,\mathbf{B}\rangle}{4\pi\rho} = \frac{\langle\mathbf{b}\rangle \times \mathrm{rot}\,\langle\mathbf{b}\rangle}{4\pi\rho} + \frac{\mathbf{B}_* \times \mathrm{rot}\,\langle\mathbf{b}\rangle}{4\pi\rho}\,. \tag{18}$$

The first term in the right-hand side describes the electromagnetic force (with the opposite sign) caused by the plasma magnetic field $\langle\mathbf{b}\rangle$. To calculate the second term, we use the obtained formula (17). We then have

$$\frac{\mathbf{B}_* \times \mathrm{rot}\,\langle\mathbf{b}\rangle}{4\pi\rho} = \frac{\big(\langle\mathbf{v}\rangle - \mathbf{v}_*\big)_\perp}{\tau}\,, \tag{19}$$

where the symbol $\perp$ denotes the velocity components normal to the magnetic field $\mathbf{B}_*$ and the characteristic relaxation time is

$$\tau = \frac{4\pi\rho\eta_{\mathrm{w}}}{B_*^2}\,. \tag{20}$$

2.3 Basic equations

To simplify the form of the equations, we omit the sign of average values in what follows. The plasma flow resulting from mass transfer in a close binary system, with the strong magnetic field $\mathbf{B}_*$ of the compact star taken into account, can be described by the system of equations

$$\frac{\partial\rho}{\partial t} + \nabla(\rho\mathbf{v}) = 0\,, \tag{21}$$

$$\frac{\partial\mathbf{v}}{\partial t} + (\mathbf{v}\nabla)\mathbf{v} = -\frac{\nabla P}{\rho} - \frac{\mathbf{b} \times \mathrm{rot}\,\mathbf{b}}{4\pi\rho} + 2(\mathbf{v} \times \mathbf{\Omega}) - \nabla\Phi - \frac{(\mathbf{v} - \mathbf{v}_*)_\perp}{\tau}\,, \tag{22}$$

$$\frac{\partial\mathbf{b}}{\partial t} = \mathrm{rot}\,\big[\mathbf{v} \times \mathbf{b} + (\mathbf{v} - \mathbf{v}_*) \times \mathbf{B}_* - \eta\,\mathrm{rot}\,\mathbf{b}\big]\,, \tag{23}$$

$$\rho T\left[\frac{\partial s}{\partial t} + (\mathbf{v}\nabla)s\right] = n^2(\Gamma - \Lambda) + \frac{\eta}{4\pi}(\mathrm{rot}\,\mathbf{b})^2\,, \tag{24}$$

where P is the pressure, s is the specific gas entropy per gram, $n = \rho/m_p$ is the particle number density, m_p is the mass of the proton, and η is the total magnetic viscosity coefficient. In equation for entropy (24), radiation heating and cooling, as well as matter heating due to current dissipation (the last term) are taken into account.

We note that the radiation heating and cooling functions Γ and Λ depend in a complex way on the temperature T (see [40–43]). In our numerical model, we use a linear approximation of these functions near the equilibrium temperature $T = 11230$ K [17, 30, 44], corresponding to the effective temperature 37,000 K of the accretor.[1] The term $2(\mathbf{v} \times \mathbf{\Omega})$ in equation of motion (22) describes the Coriolis force. The density, entropy, and pressure are related by the ideal gas equation of state $s = c_V \ln(P/\rho^\gamma)$, where c_V is the specific heat capacity of the gas at constant volume and $\gamma = 5/3$ is the adiabatic index.

The last term in equation of motion (22) describes the force acting on the plasma from the magnetic field of the acrretor; this force affects the transverse plasma velocity component $\mathbf{v}_\perp$ across magnetic field lines. We note that the motion of plasma particles is mainly determined by the compact object gravity (the gravitational drift) [45–47]. The Larmor motion of particles in the magnetic field decelerates their average motion in the transverse direction. The strong external magnetic field plays the role of an effective fluid with which plasma interacts. The last term in Eqn (10), whose form is similar to the friction force between the plasma components consisting of several sorts of particles [45], can then be treated as the friction force between the plasma and the magnetic field.

We note that a similar expression for the electromagnetic force from the magnetic field of the accretor was used in [7, 20–25], where the flow structure was modeled using the method of quasiparticles. There, individual plasma blobs entering the Roche lobe of the accretor through the inner Lagrange point L_1 were treated as quasiparticles. The authors of those papers justified the expression for the dragging force acting on the blogs in the form $-\mathbf{v}_\perp/\tau$ by pointing out that the motion of blobs in an external magnetic field leads to diamagnetic screening [48], which hampers their cross-field motion.

2.4 Magnetic field diffusion

Ohmic, ambipolar, and turbulent diffusion can lead to dissipation of the magnetic field in plasma. Because the plasma in accretion discs in CBSs is typically fully ionized, the ambipolar diffusion can be neglected. On the other hand, the turbulent diffusion coefficient is by many orders of magnitude higher than that of Ohmic diffusion [9, 49]. Therefore, in our model, Ohmic diffusion is also neglected.

It is known (see, e.g., [9]) that the turbulent diffusion of the magnetic field in accretion discs in CBSs is determined by two main effects. The first is due to magnetic reconnection and current dissipation in turbulent eddies. The diffusion coefficient due to this effect can be expressed as $\eta_T = \alpha_T c_s H$ [49], where c_s is the speed of sound, H is the half-thickness of the disk, and α_T is the Shakura–Sunyaev parameter [50] characterizing turbulent viscosity in an accretion disc. Estimating H from the vertical hydrostatic equilibrium in the disc, we obtain

$$\eta_T = \alpha_T \frac{c_s^2}{\omega_K}\,, \tag{25}$$

where ω_K is the angular rotation velocity of a Keplerian disc. The second effect is due to the buoyancy of the tubes of the toroidal magnetic field generated in the disc by differential rotation. The magnetic field diffusion coefficient due to this effect can be estimated by considering the stability of equilibrium of magnetic tubes in the disc [38]. Straightforward analysis leads to the expression $\eta_B = \alpha_B l_P |b_\varphi|/\sqrt{4\pi\rho}$, where α_B is the magnetic buoyancy efficiency coefficient of the order of unity and l_P is the scale of pressure inhomogeneity. Setting $l_P = H$, we find

$$\eta_B = \alpha_B \frac{c_s |b_\varphi|}{\omega_K \sqrt{4\pi\rho}}\,. \tag{26}$$

In systems with a strong magnetic field, the accretion disc cannot be formed at all, and the flow has the form of a column stream directed from the inner Lagrange point L_1 to the magnetic pole of the accretor. In this case, the main effect leading to the dissipation of currents in plasma appears to be the wave MHD turbulence arising due to the propagation of Alfvénic and magnetosonic waves in the accretion stream. The velocity of these waves is many times higher than the plasma velocity, and can even be relativistic in some cases. The magnetic diffusion coefficient due to the wave MHD turbulence can be estimated as

$$\eta_w = \frac{\tau_w}{3} \langle \delta\mathbf{v}^2 \rangle\,, \tag{27}$$

where τ_w is the correlation time of pulsations. This expression can be parameterized as

$$\eta_w = \alpha_w \frac{B_* l_w}{\sqrt{4\pi\rho}}\,, \tag{28}$$

where α_w is a dimensionless parameter of the order of unity that determines the wave diffusion efficiency and l_w is the characteristic space scale of pulsations, which can be taken to be equal to the inhomogeneity scale of the external magnetic field $l_w = B_*/|\nabla B_*|$. For a dipole field, $l_w \approx r/3$.

The total magnetic field diffusion coefficient is $\eta = \eta_T + \eta_B + \eta_w$. In calculations below, we have used $\alpha_T = 0.01$, $\alpha_B = 0.01$, and $\alpha_w = 0.3$. In our model, the turbulent viscosity is explicitly ignored, but the presence of numerical viscosity nevertheless allows us to take dissipative processes in the system into account. In the nonmagnetic solution, the numerical viscosity, which is due to the choice of the calculation scheme and the computational mesh, was expressed in terms of the Shakura–Sunyaev parameter and was $\alpha_T = 0{,}01$, with the same value used in the solution with the magnetic field. We note that the magnetic viscosity coefficient η_B due to magnetic buoyancy depends on the value of the magnetic field $\mathbf{b}$ in the plasma. Therefore, the turbulent diffusion of the magnetic field is nonlinear in general.

We note that the Hall effect can significantly affect the MHD flow structure in close binaries (see, e.g., [45]). This effect appears in a magnetized plasma when $\omega_B \tau_c \gg 1$, where ω_B is the Larmor frequency and τ_c is the characteristic time of electron–ion collisions (τ_c^{-1} is the collision frequency). The plasma magnetization condition $\omega_B \tau_c \gg 1$ is equivalent to

[1] The temperature is given for the specific system SS Cyg, an intermediate polar candidate.

$l \gg r_L$, where l is the free path length and r_L is the Larmor radius. With the Hall effect taken into account, Eqn (8) for the generalized Ohm law must be replaced with the equation

$$\mathbf{j} + \frac{\omega_B \tau_c}{B}(\mathbf{j} \times \mathbf{B}) = \sigma\left[\mathbf{E} + \frac{1}{c}(\mathbf{v} \times \mathbf{B})\right]. \quad (29)$$

The value τ_c^{-1} can be estimated as the effective Coulomb collision rate (taking screening at distances much larger than the Debye length into account) in a fully ionized plasma (see, e.g., [51]): $\tau_c^{-1} = 5.5T^{-3/2}n\Lambda_C$, where Λ_C is the Coulomb logarithm. Simple estimates show that the Hall effect can be important inside the accretor magnetosphere ($\omega_B\tau_c = 10^4$, $l = 2.6$ cm, $r_L = 2 \times 10^{-4}$ cm), in accretion columns of intermediate polars, and in accretion streams of polars ($\omega_B\tau_c = 25$, $l = 5.7 \times 10^{-4}$ cm, $r_L = 2.3 \times 10^{-5}$ cm), as well as, apparently, in a rarefied common envelope around the binary system. In accretion discs of cataclysmic variables (the main objects of our study), the Hall effect can be neglected for typical densities and magnetic fields ($\omega_B\tau_c = 0.0035$, $l = 8 \times 10^{-4}$ cm, $r_L = 0.02$ cm).

2.5 Numerical method

We use the Nurgush numerical code [30, 31, 33, 44]. The code is based on a finite-difference Godunov-type high-accuracy scheme. The original technique of unified variables for MHD equations [52] allows the use of adaptive grids in the numerical code. In calculations presented below, we use a geometrically adapted grid tightening to the equatorial plane and the accretor surface, which allows significantly increasing the resolution of the vertical structure of the accretion disc near the accretor magnetosphere. To minimize numerical errors in the finite-difference scheme, only the magnetic field induced by currents in the accretion disc and the external envelope is calculated [53–55]. The eight-wave method is used to clean up the magnetic field divergence [54, 56].

The magnetic field diffusion equation is nonlinear. Hence, the use of explicit methods for its solution would put too stringent a constraint on the time step size. In our approach, this equation is solved numerically using an implicit locally one-dimensional method with a factored operator [57]. In a curvilinear nonorthogonal coordinate system determined by the geometrically adaptive grid, this equation contains mixed derivatives, which is another difficulty. To circumvent this problem, our method [58] applies regularization of the factored operator. In fact, the regularization procedure is reduced to the change in operator factors that make up the original factored operator, by some equivalent three-diagonal operators. Then the regularization parameter is determined by the maximum eigenvalue of the metric tensor describing the curvilinear coordinate system. To correctly take nonlinear terms into account, an iteration process is organized in the code until a solution with the required accuracy is reached. At each iteration step, a system of linear algebraic equations with a three-diagonal matrix emerges, which is solved numerically using the scalar sweep method.

3. Gas dynamics in nonmagnetic close binary stars

3.1 General facts

After the donor star has filled its Roche lobe, the gas stream in a CBS starts in the vicinity of the libration point L_1. Away from L_1, the gas velocity increases toward the accretor, and the flow soon becomes supersonic. In addition, under the action of the Coriolis force, the stream deviates from the line connecting the component centers. The analysis of the gas trajectory shows that it comes quite close to the point mass that represents the accretor star in the Roche approximation. The minimum distance R_{min} between the trajectory of an individual particle and the accretor center for binaries with the component mass ratio in the range $0.05 < q = M_d/M_a < 1$ can be approximated by the relation [5]

$$R_{min} = 0.0488\, q^{-0.464} A\,. \quad (30)$$

For binary systems with the accretor radius $R_a < R_{min}$, the gas stream envelops the star and finally self-intersects at some point. Taking into account that the intersection point of test particles is located sufficiently close to the accretor and hence the influence of the donor star on the stream near the collision point can be neglected, we can assume that the angular momentum of a gas element relative to the accretor is conserved. For a particle with a given angular momentum orbiting around a point-mass gravitating center, the minimum energy is reached in a circular orbit, and it should therefore be expected that after the collision, a gas ring forms around the accretor. The gas rotates in the ring with the azimuthal velocity v_φ, which, in the absence of pressure gradients, is determined by the balance between the centrifugal force v_φ^2/r and the gravitational attraction of the accretor GM_a/r^2. Matching these forces yields the Keplerian rotation law $v_K = (GM_a/r)^{1/2}$. The angular momentum in such a ring increases outward as $\sim \sqrt{r}$. The obtained radial angular velocity dependence $\omega_K = v_K/r$ implies that the gas in the ring rotates differentially, i.e., nonzero shear tensions appear in the gas flow. Due to dissipative processes, a redistribution of the angular momentum across the ring, and hence the ring would finally form an accretion disc.

In the stationary case, in there is a steady matter supply into the accretion disc from the donor star with some angular momentum. Therefore, to keep a steady accretion disc, there must be a mechanism of angular momentum removal from the disc outside the system. From the physical standpoint, such a removal can be realized in two ways: either by transforming the kinetic energy of matter into another form without angular momentum conservation (for example, into thermal or magnetic field energy) or by redistributing the angular momentum when its excess is brought away into space by some matter. The need for angular momentum removal by matter becomes obvious, for example, from a consideration of the accreting ring evolution. The ring expands and its outer radius gradually increases; however, this expansion is limited by the radius of the so-called last stationary orbit, beyond which matter cannot belong exclusively to the accretor [59]. Inevitably crossing this radius, matter leaves the accretion disc and joins the circumbinary shell of the system, thus carrying away the angular momentum.

Very general assumptions therefore imply that the gas flow in nonmagnetic CBSs should include the gas stream from L_1, the accretion disc, and the circumbinary envelope. To correctly describe the flow structure and features arising from the interaction of the stream, disc, and envelope, we should solve the complete system of three-dimensional equations. Such studies have been carried out starting from papers [60–62]. In this section, we present the results of three-dimensional numerical studies of the flow structure in CBSs obtained by us in [17–19, 63–67]. We have used the TVD (total variation

diminishing) method for solving gasdynamic equations, which allows considering the morphology of gas flows in the system despite the presence of significant density gradients. The gas dynamics of mass transfer in a semidetached CBS have been studied over long time intervals, and thus the main features of the flow in the steady (relaxed) state have been found.

3.2 Morphology of the flow

The morphology of the flow in the considered systems can be seen in Fig. 1, where the density and velocity vectors are shown in the equatorial plane of the system. Shock waves formed in the disc are seen in this picture as isodensity line condensations. The isodensity lines accumulating at the edge of the accretion disc correspond to the sharp density drop from high values in the disc to low values in the circumbinary envelope.

As is evident from these results, the interaction of the circumdisc halo with the stream flowing from the L_1 point forms a bow shock, similar to the collision of two streams. The emerging structure consisting of two shocks and the tangential discontinuity between them lies outside the disc and has a complicated form. Distant parts of the circumdisc halo have a low density, and the shock wave resulting from the interaction with the gas stream is located along the edge of the stream. As the halo gas density increases, the shock wave bends and finally joins the edge of the accretion disc. Thus, the shock appears to be very extended and can be called a 'hot line'. The general picture of the flow depicted above shows that at the interaction location, the halo gas and the stream gas pass through the corresponding shocks, and the mixed flow moves along the tangential discontinuity between the two shocks. Later, this flow forms the disc, the halo, and the circumbinary shell.

The obtained numerical results allowed using the hot line to explain the form of light curves of cataclysmic variable stars. The phenomenological model used earlier assumed the presence of a 'hot spot' — a compact high-temperature region — at the edge of the disc. Numerical modeling showed that in the self-consistent treatment of the problem, the region of enhanced energy release — the hot line — has the length up to a quarter of the accretion disc perimeter. Light curves calculated in the hot-line model better correspond to observations [68–71]; in addition, some phenomena, such as dips on the light curve observed in some systems at the orbital phase ~ 0.7, can be naturally explained by our model [19].

The tidal interaction with the donor star leads to the formation of a spiral shock wave, which appears in the form of two arms located at the outer edge of the accretion disc.

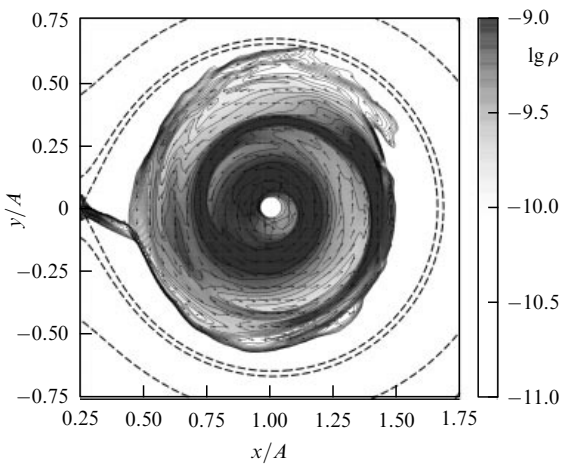

Figure 1. The distribution of density (in decimal logarithmic scale) and velocity in the equatorial plane of a typical CBS. Coordinates x and y are given in units of the distance between the components A. The accretor is shown by the white circle. The Roche equipotentials are shown by dashed lines.

3.3 Precession density wave in accretion discs

As follows from the general morphology of the flow, shocks (the hot line and two tidal spiral arms) are located at the outer edge of the disc, and hence the inner region of the disc remains virtually unperturbed. In the absence of external perturbations, a test particle in the inner parts of the disc would move around the gravitating center — the accretor — in an elliptical orbit. It is well known (see, e.g., [5]) that the effect of the secondary component in a binary system leads to a retrograde precession of the particle orbit (i.e., to the turn of the orbital semimajor axis in the direction opposite to the orbital motion), and the precession rate decreases with radius. The accretion disc consists of many particles, each moving in an individual elliptical orbit. Because the particles interact with each other and form a gas, the disc should be treated gasdynamically, and instead of individual orbits, we should consider stream lines, which are also elliptical. As in a gas, there can be no mutually intersecting streams: the stream lines can only touch each other. It is clear from geometrical considerations that nonintersecting ellipses can form a disc only if they are enclosed inside each other. For stream lines with zero eccentricity, we would obtain a circular disc. If the eccentricities of all ellipses are equal, then an 'equilibrium' solution can be realized when all semimajor axes of the stream lines are aligned. If there is an external perturbation (which is inevitable in a binary system) and orbits precess with higher rates at larger radii, the outer ellipse catches up with the inner one (with a smaller semimajor axis). Because no intersecting stream lines can exist in a gaseous disc, an equilibrium quasi-solid-body configuration precessing with some rate should ultimately be formed. This rate is intermediate between the precession rate of some limiting outer ('fast') and inner ('slow') orbits. The inner limiting orbit lies in the region where the gravitational interaction with the secondary component can be neglected. The outer limiting orbit is determined by the size of the region without gasdynamic perturbations, because perturbations would make precession of stream lines irregular. Clearly, the location of both inner and outer limiting orbits depends on parameters of the binary system and mass transfer, and therefore the mean precession rate of the disc should be different in different systems. The formation of spiral structures in accretion discs was considered in [18, 72, 73].

The analysis of the results of three-dimensional numerical calculations shown in Fig. 1 fully confirms the hypothesis of the formation of a tidal spiral wave in the inner parts of a cold accretion disc. The calculations show that the precession wave slowly turns in the laboratory (rest) frame, while its precession period in the noninertial corotating reference frame slightly exceeds the orbital period. We note that the precession wave revealed by numerical calculations is a density wave. Nevertheless, it leads to a significant redistribution of the angular momentum in the disc. The accretion rate due to the radial motion caused by the 'precession' density

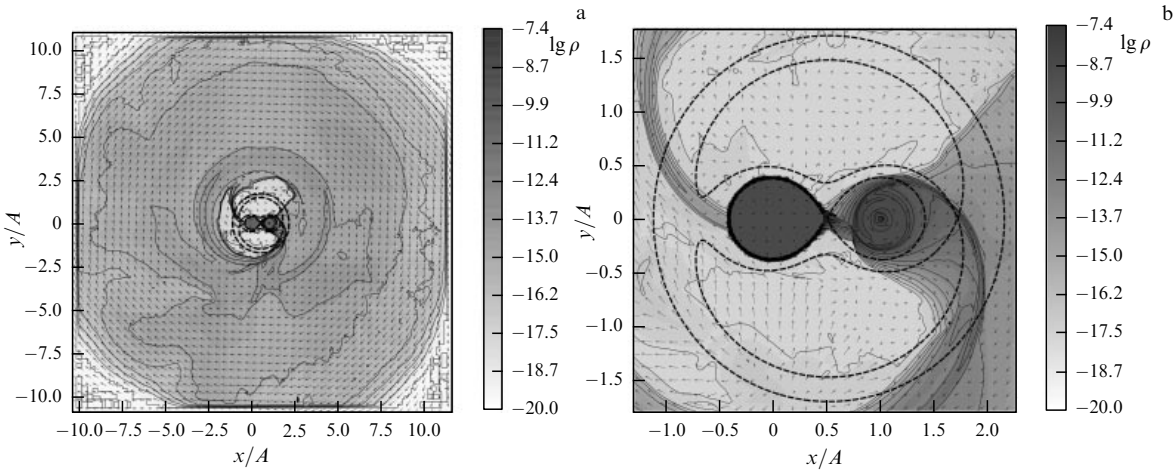

Figure 2. (a) Density distribution (in the decimal logarithmic scale) and the velocity field in the equatorial plane of the system. Equipotentials passing through points L_1 and L_3 are shown by dashed lines. The donor star center of mass is located at the point $(0, 0)$, the accretor is at the point $(1, 0)$. The orbital rotation is counterclockwise. Velocities are given in the reference frame corotating with the binary system. (b) Close-up of the inner parts of the system.

wave can increase by about an order of magnitude relative to the solution without such a wave.

3.4 Formation of the common envelope

As follows from the constructed gasdynamic model, the common envelope of a CBS is replenished by periodic matter injections from the accretion disc through the Lagrange point L_3 [74–76]. The analysis of the flow structure revealed the mechanism responsible for such injections. This mechanism is based on the interaction of the elliptical accretion disc with the external shock (ES) that emerges ahead of the disc during its orbital motion in the circumbinary envelope. The accretion disc in the system has the form of an ellipse with the accretor star located at one of its focuses. The disc shape and orientation in space are determined by the precessing spiral wave. The wave is almost at rest in the laboratory frame. Therefore, during the orbital motion of the disc, the disc apastron periodically approaches the ES, pushing it outward, or is directed oppositely, allowing the ES to approach the accretor. This motion modulates the efficiency of the angular momentum transport from the disc to the envelope, resulting in periodic mass ejections through the L_3 point and the replenishing of the common envelope.

The general shape of the obtained matter distribution in the envelope (in terms of the density distribution in a decimal logarithmic scale and the velocity field in the equatorial plane) is shown in Fig. 2a. The dashed lines show equipotentials passing through points L_1 and L_3. Figure 2b shows the density and velocity distributions in the inner part of the calculation region $(3.6A \times 3.6A)$, including both components of the system and the common envelope.

As can be seen from Fig. 2, all characteristic details of the gas flow in CBSs are formed in the inner part of the envelope: the gas stream from the inner Lagrange point L_1, the elliptical accretion disc, the external shock due to the collision of the accretion disc with the common envelope, and the spiral tail of matter ejected through the vicinity of the L_3 point. The following main structures can be seen in the common envelope: a *circumbinary envelope* with a characteristic size of several A, a *spiral tail* winding for one and half turns, a *fragmented shell* that is formed after the disruption of the spiral tail and which consists of density clumps with a characteristic size from $0.5A$ to $1.5A$, and a *diffusive disc* formed at a large distance from the CBS, where density clumps from the fragmented shell expand due to dissipative processes and form an almost homogeneous medium.

The inner part of the envelope adjacent to the binary components and the accretion disc is located at the distance less than $1.5A$ from the system barycenter. The matter in most of this region (excluding regions occupied by the stream, the accretion disc, and the vicinity of the external shock) is strongly rarefied and nonstationary, and exhibits many gasdynamic features. However, due to the low density its observational manifestations must be insignificant.

The second part of the common envelope located at a distance $\sim (1.5-7.5)A$ from the system barycenter includes a rather dense spiral tail counting one and a half turns (its density is several percent of the disc density). The tail is formed by matter expelled through the vicinity of the L_3 point. At a distance $\sim (7-8)A$, the spiral structure is destroyed and transforms into a fragmented ring-like shell, which extends to about $10A$. At larger distances, the fragmented shell transforms into an extended diffusive disc with the thickness-to-radius ratio $H/r \simeq 0.1$.

The common envelope density depends on the amount of injected matter, which can be estimated by the formula $\dot{M}(1 - \dot{M}_{\rm a}/\dot{M})$, where $\dot{M}$ is the mass exchange rate, $\dot{M}_{\rm a}$ is the mass accretion rate, and $\dot{M}_{\rm a}/\dot{M}$ is the accretion efficiency. The accretion efficiency depends on the rate of angular momentum removal. In the considered numerical model, the value of the Shakura–Sunyaev $\alpha_{\rm T}$ parameter is ~ 0.01, which yields the accretion efficiency $\sim 30\%$. As the modeling shows, with the adopted accretion efficiency and at the mass exchange rate $\dot{M} > 10^{-8} M_{\odot}$ y^{-1}, the common envelope should be optically thick in the equatorial plane, and it must therefore be taken into account in the interpretation of observations.

4. Structure of the MHD flow

4.1 Parameters of the model star

We study the effect of the accretor magnetic field on the flow structure in CBSs using the parameters of SS Cyg as a

template (see, e.g., [77]). The donor star (a red dwarf) in this system has the mass $M_d = 0.56M_\odot$ and an effective temperature of 4000 K. The accretor star (a white dwarf) has the mass $M_a = 0.97M_\odot$ and a temperature of 37,000 K. The orbital period of the binary system is $P_{orb} = 6.6$ h and the distance between the components is $A = 2.05R_\odot$. The inner Lagrange point L_1 is located at a distance of $0.56A$ from the accretor. A large amount of information about the system has been obtained over more a than hundred years of observations. However, many issues relating to the physical properties of the system remain open. Morphological features allow SS Cyg to be classified as a U Gem type star. But there are indications that SS Cyg is an intermediate polar with the magnetic field $B_a = 10^4 - 10^6$ G [78, 79]. The presence of the magnetic field significantly affects the flow, and it must therefore be taken into account in order to understand the properties of the system.

The spin period of the accretor in SS Cyg [80] for the assumed binary inclination angle $i = 40°$ [81] is $P_{spin} = 68.4$ s $= 0.0029P_{orb}$. The accretor rotation is characterized by the spin period $P_{spin} = (1 + \Omega_*/\Omega)^{-1}P_{orb}$ and is an important factor that must be taken into account in modeling binary systems with steady accretion discs. The characteristic time scale P_{spin} of the spin change in such systems can be estimated from the characteristic time scale of the white dwarf angular momentum increase due to the accretion of matter from the inner parts of the disc [8]:

$$t_A \approx \left(\frac{R_a}{A}\right)^2 \sqrt{\frac{(1+q)A}{R_{in}}}\,\frac{M_a}{\dot{M}_a}\,, \tag{31}$$

where R_{in} is the inner radius of the disc. For typical parameters of intermediate polars, we find the time t_A of the order of $10^4 - 10^5$ years. The spin-down torque due to the magnetic field leading to the equilibrium acretor spin period can increase this estimate.

We consider a CBS in which an accretion disc is being formed. The characteristic time it takes for the stationary regime to set in ranges from 10 to 15 orbital periods [17]. We can therefore neglect the change in the angular velocity of the star during disc formation. As the first step, it is worth considering an accretor spinning synchronously with the orbital period, $P_{spin} = P_{orb}$, at the beginning of the mass transfer. The influence of the accretor spin on the structure of an already formed disc is considered in Section 4.6.

The degree of influence of the magnetic field on the flow structure can be determined using estimates of the radius of the accretor magnetosphere. We assume that the magnetic pressure at the magnetosphere boundary is equal to the dynamic pressure of the accreting gas (see [8]):

$$\frac{B^2}{8\pi} = \rho v_{ff}^2\,, \tag{32}$$

where $v_{ff} = \sqrt{2GM_a/r}$ is the free-fall velocity. The matter density is found from the mass accretion rate $\dot{M}_a = 4\pi r^2 \rho v_{ff}$. Substituting $B = B_a(R_a/r)^3$ in (32), we obtain the magnetosphere radius

$$r_m = \left(\frac{B_a^4 R_a^{12}}{8GM_a\dot{M}_a^2}\right)^{1/7}. \tag{33}$$

The dependence of the magnetosphere radius r_m on the accretor surface magnetic field is shown in Fig. 3. Different lines correspond to different mass accretion rate $\dot{M}_a$ in units of $M_\odot$ per year. The thin horizontal lines show the accretor radius set equal to $0.0125A$ in our calculations (the bottom line) and the distance to the inner Lagrange point, set equal to $0.56A$ (the upper line). In calculations discussed below, the mass accretion rate is assumed to be $10^{-10}M_\odot$ y^{-1}. In this case, the magnetosphere radius is about $(5-6)R_a$ for the surface field $B_a = 10^5$ G and $20R_a$ for the surface field $B_a = 10^6$ G. For the magnetic field $B_a = 10^4$ G, the magnetosphere radius turns out to be smaller than that of the 'numerical star', but still larger than the white dwarf radius.

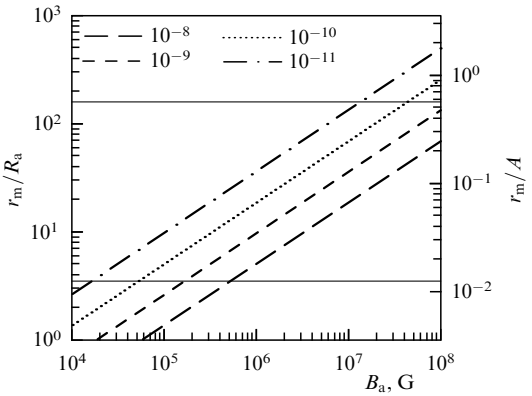

Figure 3. The magnetosphere radius of the white dwarf in SS Cyg as a function of the surface magnetic field. Different bold lines correspond to different mass accretion rates (in units $M_\odot$ y^{-1}). The thin horizontal lines show the numerical boundary of the accretor to be $0.0125A$ (the bottom line) and the distance from the accretor to the inner Lagrangian point to be $0.56A$ (the upper line).

4.2 Ideal MHD

We discuss the results of calculations of the flow structure in the ideal MHD approximation ignoring the magnetic field diffusion. In these calculations, the surface magnetic field of the white dwarf is taken to be $B_a = 10^5$ G and the inclination angles of the magnetic dipole axis are taken to be $\phi = 0°$ and $\theta = 30°$. We recall that this value of ϕ corresponds to synchronous rotation of the accretor. The structure of the MHD flow in this case at the time $t = 10.7P_{orb}$ is shown in Fig. 4.

We note that the magnetic field dominates in these calculations because the plasma parameter $\beta = 8\pi P/B^2$, which is the ratio of the gas pressure to the magnetic pressure, changes in the accretion disc from 10^{-3} to 10^{-2}, and falls to low values $10^{-5} - 10^{-6}$ in the accretor magnetosphere. The magnetic field generation study and its structure are discussed in more detail in Section 5 below. Here, we only note that the magnetic field in the disc is predominantly toroidal. At the time of steady flow formation, the induced magnetic field $\mathbf{b}$ in the outer parts of the disc exceeds the original field of the white dwarf $\mathbf{B}_*$ by more than 100 times.

In spite of the magnetic field dominance, all basic elements of the accretion disc structure noted above for the purely gasdynamic case also emerge in the magnetic case. This can be explained by the formation of these structures being mainly due to gravitational effects and the pressure of the toroidal magnetic field adding to gas pressure where necessary. The two-arm spiral wave is formed due to the tidal interaction with the donor star [82]. The location of shock fronts can slightly change due to the difference in the gasdynamic and MHD shocks. The region of hot line

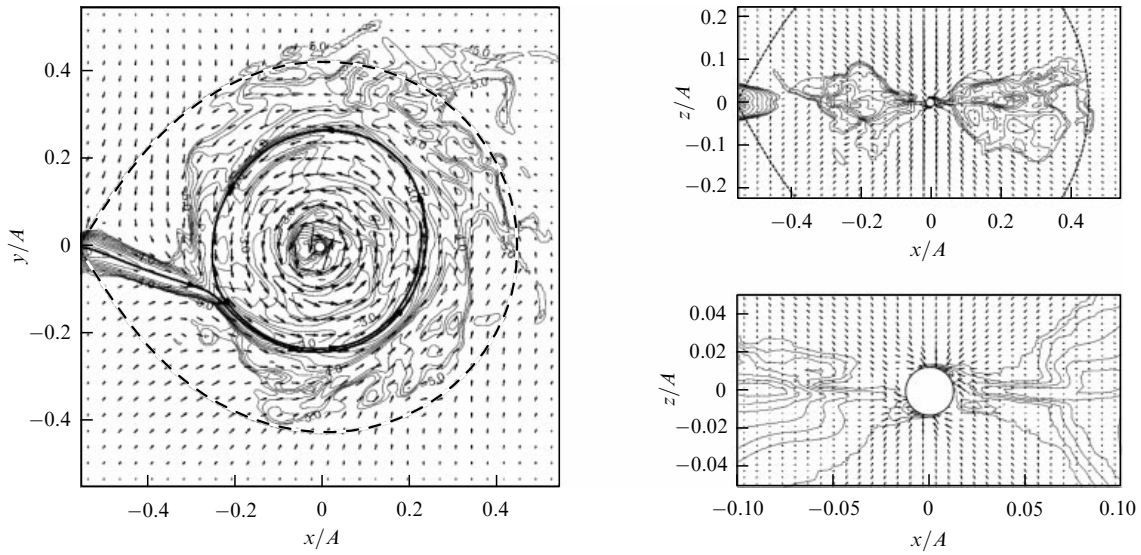

Figure 4. The density and velocity distribution in the equatorial (xy) and vertical (xz) planes in the presence of a magnetic field in the ideal MHD approximation. The density logarithm is shown on some isolines. The dashed line corresponds to the Roche lobe. The bold line with arrows shows the stream line starting at the inner Lagrange point.

formation is barely shifted because the magnetic field strength in the stream near the inner Lagrange point L_1 is close to zero. The formation of the spiral precessing wave is caused by purely gravitational effects in the inner parts of cold accretion discs [18]. Thus, this wave is also formed in magnetized discs.

We note the most significant difference in the structure of the MHD flow from the purely gasdynamic case. Due to the magnetic braking of rotation in the disc, the accretion rate increases by more than two times with respect to the nonmagnetic case, where it is about 20–30% of the mass exchange rate. As a result, the mass of the accretion disc in the magnetic case is almost four times smaller than in a nonmagnetic disc ($\approx 3 \times 10^{-12} M_{\odot}$). The radius of the nonmagnetic disc is about $0.3A$, while that of the magnetic one is $0.2A$. Hence, the characteristic gas density in the magnetic disc is an order of magnitude smaller than in a purely gaseous disc (10^{-7} g cm^{-3}). The formation of an extended rarefied halo around the disc is another feature.

The vertical structure of magnetic accretion discs is mainly determined by the toroidal magnetic field pressure gradient and not by the gas pressure gradient, because the plasma parameter $\beta \ll 1$ almost everywhere in the disc. In the magnetic case, the disc thickness significantly increases due to the magnetic buoyancy. This result can be understood from simple considerations. The total pressure is $P_{\rm tot} = P + \mathbf{B}^2/(8\pi) = (1 + 1/\beta)P$, and therefore the characteristic height of a magnetized disc is

$$H_{\rm m} \approx \sqrt{\frac{P_{\rm tot}}{\rho}}\,\omega_{\rm K}^{-1} \approx \sqrt{1 + \frac{1}{\beta}}\,H_{\rm g}\,, \qquad (34)$$

where $H_{\rm g}$ is the characteristic thickness of a gaseous disc. For $\beta \ll 1$, we obtain $H_{\rm m} \approx H_{\rm g}/\sqrt{\beta}$. Hence, depending on the plasma parameter $\beta = 10^{-3} - 10^{-2}$, the magnetic disc height $H_{\rm m}$ must be 10–30 times larger than the gas disc height $H_{\rm g}$.

Several MHD instabilities can develop in an accretion disc with a strong toroidal magnetic field. The most important among them is the magnetorotational instability discovered by Velikhov [14] and applied to astrophysical discs by Balbus and Howley [15]. When the toroidal field strongly exceeds the poloidal one, a magnetorotational-type instability, studied in [83], emerges. Numerical studies of such an instability emerging in supernova explosions were carried out in [84]. Finally, the instability due to the buoyancy of the toroidal magnetic field tubes can develop in a magnetized disc [38]. These instabilities are reviewed, e.g., in [85]. We note that all these instabilities lead to the generation of a small-scale poloidal field from the toroidal one. In our numerical model, the magnetic buoyancy is explicitly taken into account in the corresponding magnetic field diffusion coefficient [see (26)], and there are no formal prohibitions on the magnetorotational instability development. The analysis of numerical results suggests that the magnetorotational instability appears in the accretion disc regions where the corresponding criterion is satisfied. However, this instability does not propagate across the disc. This, for example, can be due to a relatively high viscosity $\alpha_{\rm T} \approx 0.01$ in the numerical solution (see Section 2.4), which corresponds to observations.

Near the white dwarf surface, the accretion in the magnetosphere proceeds via an accretion column. The characteristic size of this region is $0.02A$, which corresponds to about six white dwarf radii. This size is in good agreement with estimates of the accretion disc inner radius in SS Cyg (5.2–6.5 white dwarf radii) inferred from the observed Doppler tomograms [86]. The megnetospheric flow near the white dwarf surface is shown in Fig. 5. The matter moves predominantly along magnetic field lines, forms an accretion column, and falls onto the star surface in regions of the magnetic poles. The magnetic field of the star becomes significantly distorted because the toroidal magnetic field is intensively generated near the disc–magnetosphere boundary. Vacuum regions appear near the magnetic equator. They are formed because the magnetic field prevents matter from penetrating into the magnetic equator region, where magnetic field lines run predominantly parallel to the star surface.

4.3 Effect of the magnetic field diffusion on the solution

Due to magnetic field diffusion, the flow structure becomes intermediate between the purely gasdynamic case and the ideal MHD case. We compare the calculated MHD flow

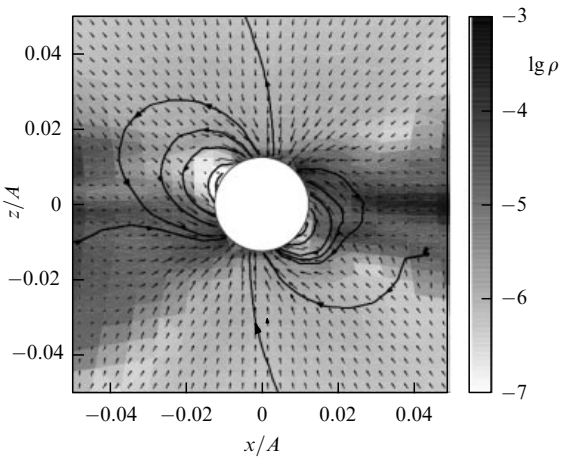

Figure 5. The distribution of density, velocity (arrows) and the magnetic field structure (bold lines with arrows) in the accretor magnetosphere in the vertical plane (xz) near the time $10.7P_{\rm orb}$ in the ideal MHD case.

without (model A) and with (model B) magnetic field diffusion [31]. Figure 6 shows the density and velocity distribution in the equatorial (xy) and vertical (xz) planes near the time the steady state sets in $(t = 13.4P_{\rm orb})$. The notation in this figure is the same as in Fig. 4.

All features of the flow discussed in Section 4.2. for model A are also present in model B. Differential rotation in the accretion disc leads to an intensive magnetic field generation. In both models, the magnetic field turns out to be dominant in the accretion disc because the plasma parameter β is smaller than unity. As noted above, in model A, $\beta \approx 10^{-3}$. In model B, the plasma parameter increases by two orders of magnitude $(\beta \approx 0.1)$. In both cases, the plasma parameter decreases to extremely low values $10^{-5} - 10^{-6}$ inside the accretor magnetosphere. In model B, magnetic field growth is restricted mainly by the magnetic buoyancy, since the corresponding diffusion coefficient depends on the toroidal magnetic field [see (26)].

The magnetic field **b** in the accretion disc is predominantly toroidal. In the obtained steady-state solution, the absolute value of **b** in the outer parts of the disc exceeds the magnetic field B_* by more than 100 times. Figure 7 shows the azimuthally averaged toroidal B_φ and poloidal $B_{\rm p}$ components of the total magnetic field **B** in the equatorial plane of the accretion disc in both models. The characteristic value of the magnetic field in the middle parts of the accretion disc is 200 G in model A and about 50 G in model B.

The accretion disc in model B is about three times more massive than in model A. The outer disc radius in models A and B is respectively $0.2A$ and $0.3A$. The characteristic disc density in model A is $10^{-3}\rho(L_1)$, which is substantially smaller than in model B $(5 \times 10^{-2}\rho(L_1))$. The vertical structure of the magnetic disc is determined by the total pressure gradient [see (34)]. Using the corresponding values of the plasma parameter β, we obtain the estimates $H_{\rm m} \approx 30H_{\rm g}$ for model A and $H_{\rm m} \approx 3H_{\rm g}$ for model B. Therefore, the magnetic field diffusion can significantly decrease the disc thickness (by an order of magnitude or even more).

The characteristic magnetosphere radius in both models is approximately $0.02A$, which corresponds to about six white dwarf radii and is in agreement with observations [86]. On the other hand, this value is also in agreement with analytic estimates obtained from formula (33). The flow structure in the magnetosphere region is almost the same in both models (see Figs 5 and 8). In this region, plasma moves along the magnetic field lines and falls onto the accretor at the magnetic poles. The region with a strongly rarefied plasma is formed near the magnetic equator. The reason is that the plasma velocity is almost parallel to the accretor surface in this zone.

Figure 9 shows the dependence of the accretion rate $\dot{M}_{\rm a}$ on time during the last several orbital periods in both models. This dependence differs greatly in different models. In the ideal MHD case (model A), the accretion rate shows strong irregular variations. The mean accretion rate in this model is approximately equal to the mass exchange rate $\dot{M} = 10^{-9} M_\odot\ {\rm y}^{-1}$, with the amplitude of oscillations reaching $1.5 \times 10^{-9} M_\odot\ {\rm y}^{-1}$. The maximum accretion rate can be two times higher than the mass exchange rate. The turbulent diffusion decreases the mass accretion rate twofold and significantly smoothes out its variations. This can be explained as follows. In the ideal MHD case, the magnetic field in the accretion disc is sufficiently strong. Therefore, the

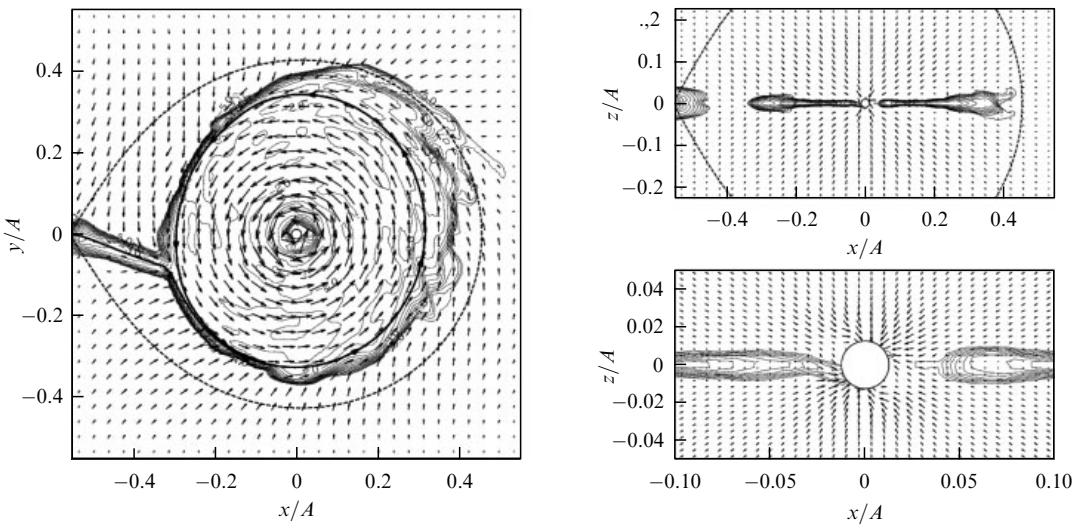

Figure 6. The density and velocity distribution in the equatorial (xy) and vertical (xz) planes in the magnetic case with the magnetic field diffusion taken into account. The notation is the same as in Fig. 4.

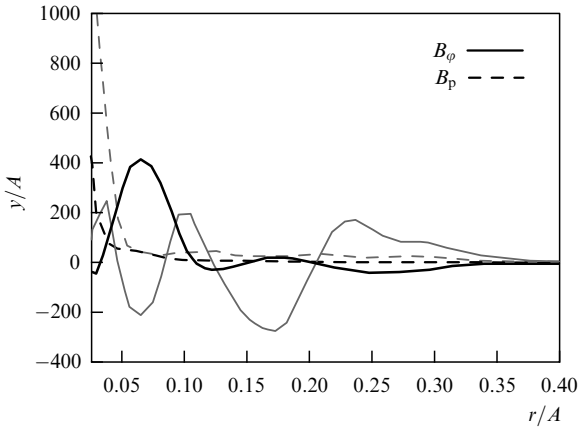

Figure 7. The azimuthally averaged toroidal B_φ and poloidal B_p magnetic fields in the equatorial plane of the accretion disc for model A (thin lines) and model B (bold lines).

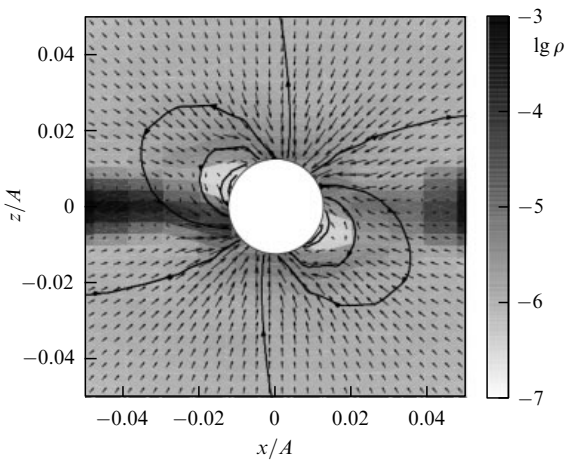

Figure 8. Density and velocity (arrows) distributions and the magnetic field structure (bold lines with arrows) in the accretor magnetosphere in the vertical plane (xz) near the time $10.7P_{\rm orb}$ in the model that takes the magnetic field diffusion into account.

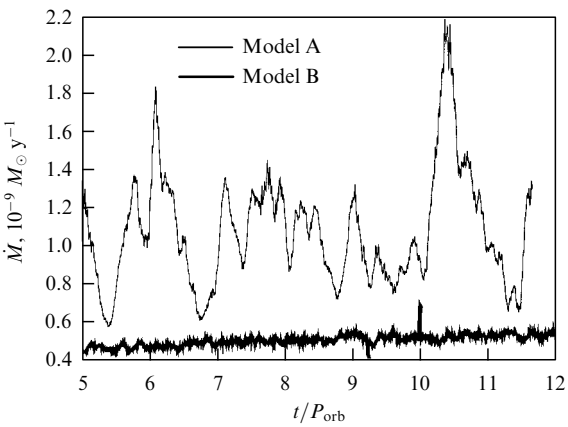

Figure 9. Evolution of the accretion rate over the last several orbital periods.

angular momentum is effectively transported from outer parts of the disc by magnetic braking. In addition, the magnetic field diffusion can spread out the column flow and hence smooth out the accretion rate variations.

We consider the evolution of the mass accretion rate onto a compact star over several orbital periods (see Fig. 9). The maximum amplitude of the accretion rate variations in model B is about 15–25%. In the ideal MHD case (model A) without diffusion effects, the amplitude of these variations can exceed 200%. The UV flux from SS Cyg between outbursts demonstrates a very similar behavior (see [87]). The flux variations reach 70%. There are several possible mechanisms responsible for the accretion rate variations. One is related to the quasiperiodic character of the magnetic field generation in the disc and is described in more detail in Section 5. Another possible mechanism can be due to the interaction of the white dwarf magnetic field with the spiral precessing wave formed in the inner parts of the disc. In the gasdynamic case, the increase in the radial flow of matter behind this wave leads to an increase in the accretion rate and enhanced energy release on the accretor surface [18]. In the magnetic case, the accretion occurs via an accretion column. However, when a precession wave approaches a white dwarf surface near the magnetic poles, the accretion rate must increase. In the corotating reference frame, the rotational period of the spiral wave is approximately equal to (larger by several percent than) the binary orbital period. Therefore, spikes in the mass accretion rate should be observed nearly twice as often in the orbital period when the spiral density wave passes near the north and south magnetic poles of the accreting star.

4.4 Flow structure for different magnetic fields

To study the effect of the accretor magnetic field on the flow structure in CBSs, calculations were carried out for the field ranging from 10^5 to 10^8 G [33]. We consider seven models of the accretor magnetic field: 10^5 G (model 1), 5×10^5 G (model 2), 10^6 G (model 3), 5×10^6 G (model 4), 10^7 G (model 5), 5×10^7 G (model 6), and 10^8 G (model 7).

These models can be divided into two groups. The first includes models 1, 2, and 3 with relatively weak magnetic fields, in which an accretion disc is formed. In the second group, including models 4–7, the magnetic field is strong and the accretion disc is not formed. The second group corresponds to polars. In all models, calculations continued until steady-state conditions were established; this state was identified by a constant (to within 1%) amount of the total mass in the calculation region. In models with an accretion disc, it took about 10–15 orbital periods for the steady state to be reached. In models with a strong magnetic field without an accretion disc, a quasistationary state was reached in a shorter time (about five orbital revolutions). We discuss the results of calculations for these two model groups separately.

The 3D structure of the flow in models 1–3 is demonstrated in Fig. 10. In this figure, isodense surfaces (on a logarithmic scale) $\lg \rho = -4.5$ [in units $\rho(L_1)$] and magnetic field lines beginning on the accretor surface are presented. The intensity of the gray color of magnetic lines corresponds to the magnetic field strength. The accretor spin axis (the thin straight line) and magnetic axis (the bold slanted line) are also shown.

For $B_a = 10^5$ G (model 1), the flow corresponds to the case described in the preceding section. For $B_a = 5 \times 10^5$ G (model 2), the outer radius of the accretion disc becomes much smaller (about $0.15A$). The magnetic braking efficiency and the angular momentum transfer rate increase. The size of the magnetosphere region significantly increases. Accretion columns near the white dwarf surface become more pronounced. Finally, for $B_a = 10^6$ G (model 3), the accretion disc

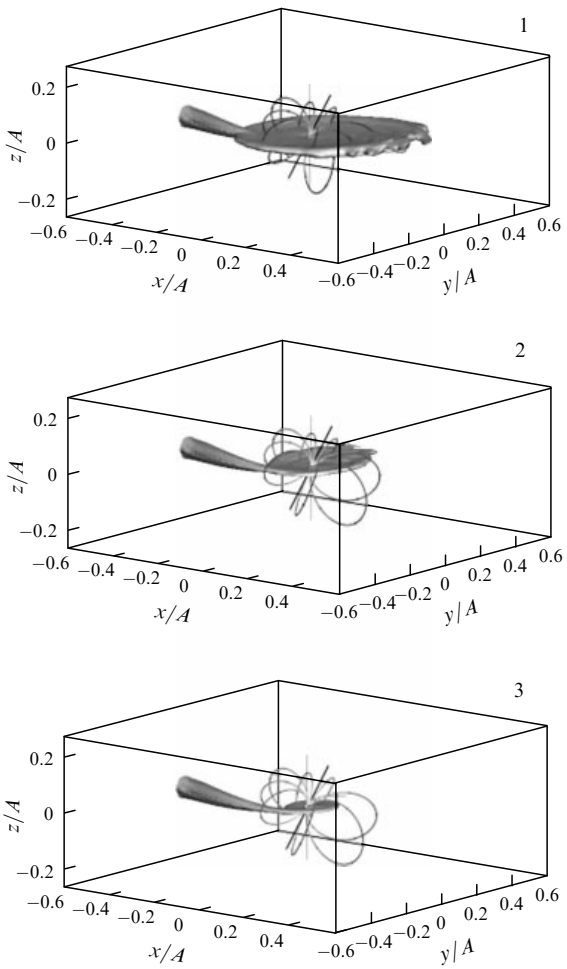

Figure 10. 3D structure of the model flows. 1 — $B_a = 10^5$ G, 2 — $B_a = 5 \times 10^5$ G, and 3 — $B_a = 10^6$ G. Isodensity surface ($\lg \rho = -4.5$) and magnetic field lines are also shown. The color of magnetic field lines corresponds to the magnetic field strength. The thin straight line shows the spin axis and the bold slanted line shows the magnetic axis of the accretor.

is almost degenerate. The matter makes only 1–2 turns before falling onto the accretor. To describe such a structure, the term 'spiralodisc' seems to be more appropriate, because the velocity of matter in such a disc strongly deviates from the Keplerian value. The outer radius of such a spiralodisc is about $0.1A$. It is almost entirely inside the accretor magnetosphere. Accretion columns occupy a significant part of the spiralodisc. This case is very much like the limiting case of intermediate polars. We note that the magnetosphere size obtained in numerical simulations is in good agreement with analytic estimates (33) (see Fig. 3).

The structure of the MHD flow for other models is shown in Fig. 11: 4 with $B_a = 5 \times 10^6$ G, 5 with $B_a = 10^7$ G, 6 with $B_a = 5 \times 10^7$ G, and 7 with $B_a = 10^8$ G. The isodense surface of the logarithmic density $\lg \rho = -5$ [in units of $\rho(L_1)$] and magnetic field lines are shown. As in Fig. 10, the gray scale corresponds to different magnetic field strengths. The spin axis (the thin line) and the magnetic axis (the bold line) of the accretor are also shown. The image is turned such that features of the accretion flow near the white dwarf surface are visible.

The analysis of these figures shows that the flow structure in models 4–7 is qualitatively different from that in models 1–3. In models 4–7, the accretion disc is not formed and accretion proceeds through a column. In models 4 and 5, the stream beginning at the inner Lagrange point L_1 is split into two flows accreting onto the north and south magnetic poles. In model 4, the north stream dominates, while in model 5, the south stream is stronger. The magnetic field is weaker in model 4, and hence the ballistically moving stream is captured by the magnetic field at a point lying closer to the north magnetic pole. In model 5, the field is stronger and the stream is captured by the field earlier. As in our model, the south pole of the accretor lies closer to the Lagrange point L_1; the motion of plasma in a strong magnetic field toward the south pole turns out to be energetically more favorable. This observation is confirmed in model 6 with a stronger magnetic field, in which only one gas stream onto the south pole is formed.

In the last model, 7, the magnetic field is so strong that it almost totally controls the flow inside the accretor Roche lobe. Almost immediately after the Lagrange point, the matter is captured by the magnetic field and is canalized along the magnetic field lines toward the white dwarf surface, with the more powerful stream falling onto the south pole and the less powerful one onto the north pole. In this case, the magnetosphere is larger than the accretor Roche lobe and hence partially encloses the donor envelope.

Therefore, according to our calculations of the flow structure in a CBS with the parameters of SS Cyg, an accretion disc is formed in models with the magnetic field $B_a \leqslant 10^6$ G, and no disc is formed for stronger magnetic fields. This result can be explained by the following simple considerations. Because the flow in the stream is supersonic, the behavior of matter moving from the inner Lagrange point L_1 into the Roche lobe can be studied using the ballistic approximation and ignoring the pressure and magnetic field effects [4, 6]. The analysis of trajectories [3] shows that the stream approaches the accretor at the distance $R_{\min}$ in (30). If $R_{\min}$ exceeds the magnetosphere radius r_m [see (33)], the magnetic field does not significantly affect the motion of matter. The flow can bypass the star and ultimately intersect itself at some point. The subsequent evolution of such a flow leads to the formation of an accretion disc in the system. If the minimum distance $R_{\min}$ is smaller than the magnetosphere radius r_m, then at some part of the trajectory, the flow turns out to be in the region of significant magnetic field influence. The action of the electromagnetic force in this zone brakes the flow and removes its angular momentum. As a result, the flow cannot bypass the star and forms an accretion disc. Therefore, the boundary between intermediate polars (accretion discs are formed) and polars (accretion discs are not formed) is determined by the relation $r_m = R_{\min}$. Substituting the parameters of SS Cyg here, we find the magnetic field value $B_a \approx 10^6$ G that separates the two states. Actually, this estimate of the magnetic field strength separating intermediate polars and polars is very general, because the mass ratio q in cataclysmic variables varies insignificantly around the mean value 0.5.

Figure 12 shows the dependence of the accretion rate $\dot{M}_a$ on the accretor surface magnetic field B_a. The vertical bars show the characteristic variations of the mass accretion rate. The main feature of this dependence is its nonmonotonic character. For $B_a < 10^6$ G, the accretion rate increases as the magnetic field increases, and its variation amplitude decreases. At $B_a = 10^6$ G, a maximum accretion rate is obtained. For the magnetic field B_a increasing further, the accretion rate decreases.

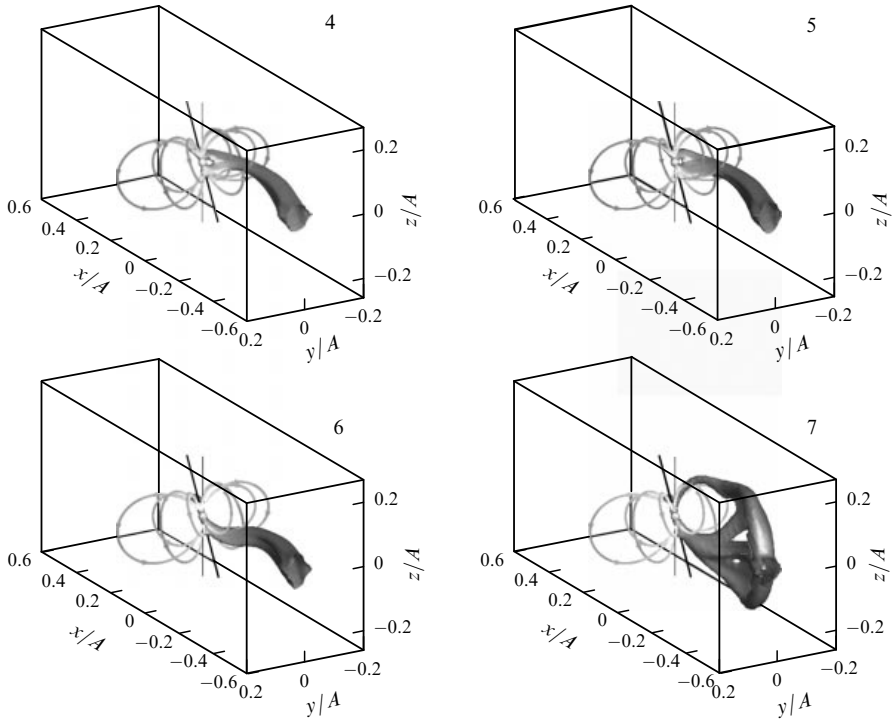

Figure 11. 3D structure of the model flows. 4 — $B_a = 5 \times 10^6$ G, 5 — $B_a = 10^7$ G, 6 — $B_a = 5 \times 10^7$ G, and 7 — $B_a = 10^8$ G. Shown are isodensity surfaces ($\lg \rho = -5$). The other notation is the same as in Fig. 10.

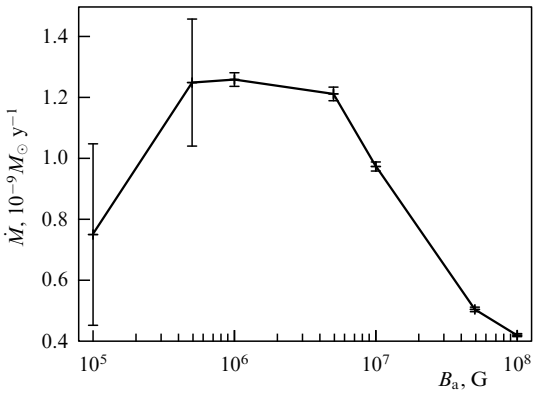

Figure 12. The dependence of the accretion rate on the surface magnetic field of the accretor B_a. Vertical bars show characteristic variations of the accretion rate.

This dependence fully corresponds to the above considerations. For $B_a < 10^6$ G, an accretion disc is formed and the accretion rate is determined by the efficiency of angular momentum transfer in the disc. The increasing magnetic field strengthens the magnetic braking in the disc. Therefore, the dependence $\dot{M}_a(B_a)$ is increasing for $B_a < 10^6$ G. Starting from the magnetic field strength $B_a = 10^6$ G, no accretion disc is formed any more, and the accretion proceeds through a column stream. In that case, the mass accretion rate $\dot{M}_a$ is determined by the ability of matter to flow through the column. Upon further increasing the magnetic field, the cross section of the stream decreases and the accretion rate decreases correspondingly.

4.5 The case of complex (multipole) magnetic fields

We study the flow structure in a CBS with an accretor surface magnetic field with a complex geometry. We consider a system with parameters similar to those of BY Cam (see, e.g., [35]). The donor star (red dwarf) in this system has the mass $M_d = 0.5 M_\odot$ and the effective temperature 4000 K. The accreting star (white dwarf) has the mass $M_a = 1 M_\odot$ and the temperature $\sim 40{,}000$ K. The binary orbital period is $P_{orb} = 3.36$ h and the distance between the components is $A = 1.3 R_\odot$. The inner Lagrange point L_1 is located at a distance of $0.57A$ from the accretor center.

The magnetic field on the white dwarf surface in BY Cam as derived from observations is 2.8×10^7 G [35]. It is assumed that the magnetic field is a superposition of the dipole and quadrupole components. In the calculations discussed below, we assume that the dipole and quadrupole symmetry axes coincide. The inclination angle of the magnetic field to the accretor spin axis is 30°. The quadrupole component is taken to be $B_{q,a} = 10 B_{d,a}$, i.e., ten times larger than the dipole component on the magnetic equator. Then the radius of influence of the quadrupole field (the distance where B_d is equal to B_q) is $r = 10 R_a$. The flow structure is modeled separately for different angles ϕ characterizing the projection of the magnetic field axis on the binary orbital plane.

The 3D structure of the flow calculated for different angles ϕ is presented in Fig. 13. Shown are surfaces of equal density -6, -4, and -2 [on a logarithmic scale, in units of $\rho(L_1)$]. The magnetic field is shown by lines with arrows. The accretor spin and magnetic axes are respectively shown by the thin straight line and the bold inclined line.

It is seen from this figure that the structure of the flow in the system essentially depends on the accretor magnetic field orientation relative to the donor. At $\phi = 0°$ (Fig. 13a), the accretion stream from the inner Lagrange point L_1 falls on the accretor in a magnetic belt that appears due to the presence of the quadrupole component. An accretion ring is then formed around the accretor. In addition, there are two streams falling

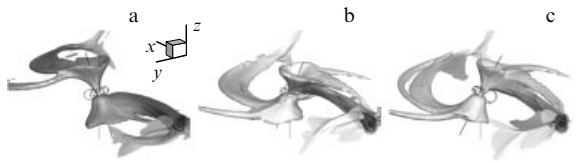

Figure 13. 3D flow in a close binary system with a complex magnetic field of the accretor for different values of the magnetic axis angle relative to the donor: (a) 0°, (b) 180°, and (c) 252°. Shown are isodensity surfaces −6, −4, and −2 [in logarithmic units of $\rho(L_1)$]. Also shown are magnetic field lines (lines with arrows) , the accretor spin axis (the thin straight line), and the magnetic symmetry axis (the bold slanted line).

directly on the north and south magnetic poles, but these flows are much weaker than the main flow.

At $\phi = 180°$ (Fig. 13b), the main accretion stream is split into two flows. One falls onto the accretor in the magnetic belt region and the other falls onto the north magnetic pole. The flows have almost equal intensities. Thus, two equally luminous zones (the north pole and the magnetic belt) appear on the accretor surface in this case.

At $\phi = 252°$ (corresponding to the orbital phase 0.7) (Fig. 13c), there are no accretion flows onto the magnetic belt, and almost all matter falls onto the north magnetic pole. This picture is similar to what is observed in polars (see Section 4.4), where the accretor has a purely dipole magnetic field.

Thus, the analysis of calculations shows that the flow structure in a close binary system can be significantly different depending on the orientation of the magnetic axis of the accretor relative to the donor. Different configurations of accretion flows and accretion zones are possible, which can change the observational properties of the system. We emphasize that the radiation from the hot spot near the magnetic pole is strongly polarized because the magnetic field has a certain direction in that region. At the same time, the radiation from the accretion belt is not polarized because the magnetic field has no distinct direction in the belt.

4.6 The case of asynchronous rotation of the accretor

The effect exerted by the proper rotation of the accretor on the MHD flow in CBSs can be characterized by the ratio of the magnetosphere radius r_m, Eqn (33), to the corotation radius r_c. The corotation radius is defined as the distance where the rotation velocity of accretor magnetic lines is equal to the velocity of matter in the accretion disc. Assuming that the magnetosphere rotates as a solid body with an angular velocity Ω_* and the angular velocity of matter in the disc is Keplerian, ω_K, we find [8]

$$r_c = \left(\frac{GM_a}{\Omega_*^2}\right)^{1/3}. \tag{35}$$

If the accretor spins sufficiently slowly ($r_c > r_m$), then the angular velocity of magnetic field lines at the magnetosphere boundary is smaller than the Keplerian value. Therefore, the matter captured by the magnetic field can freely fall onto the surface. This state can be called 'accretor'. In the case of fast magnetosphere rotation ($r_c < r_m$), the centrifugal barrier appears at the magnetosphere boundary, preventing matter from freely falling onto the accretor surface. This state was called 'propeller'. In this case, the accretion becomes nonstationary [29, 88, 89]. In the equilibrium state, $r_c = r_m$. The analysis in [8] shows that the interaction of the accretor magnetosphere with the disc makes the system gradually evolve toward the equilibrium rotation.

Table 1. Model parameters in calculations of an asynchronously spinning accretor. Parameters are given for SS Cyg. The prototypes correspond to the classification of intermediate polars currently used [7].

Model	Prototype	P_{spin}/P_{orb}	r_c/r_m	State
1	Synchronous	1	∞	accretor
2	EX Hya	0.1	1.48	accretor
3	Regular	0.033	1.00	equilibrium spin
4	DQ Her	0.01	0.66	propeller
5	AE Aqr	0.001	0.31	propeller

This classification corresponds to the observed distribution of intermediate polars over the accretor spin periods [7] (see Table 1). Most white dwarfs in these systems have equilibrium spin periods (regular intermediate polars). The accretors are divided into synchronous intermediate polars ($P_{spin} \approx P_{orb}$) and EH Hya systems ($P_{spin} \approx 0.1P_{orb}$). Fast rotators can be divided into DQ Her systems ($P_{spin} \approx 0.01P_{orb}$) and AE Aqr systems ($P_{spin} \approx 0.001P_{orb}$). Accretion discs are formed in DQ Her systems, but the propeller state is realized. In AE Aqr systems, the accretor spin is so fast that the accretion disc is not formed. In this case, the term 'superpropeller' can be used.

To study the effect of asynchronous rotation of the accretor on the flow structure in CBSs, three-dimensional numerical calculations for different period ratios P_{spin}/P_{orb} were carried out. The parameters of the models are listed in Table 1. The specific values are taken for SS Cyg. However, different models fully correspond to the intermediate-polar type described above. In all models, the surface magnetic field strength was set equal to 10^5 G and the magnetic field inclination was taken to be $\theta = 30°$.

We note that model 1 (synchronous rotation) is equivalent to model 1 (for $B_a = 10^5$ G) in Section 4.4. The flow structure in model 3 (equilibrium rotation) is only slightly different from that in model 2 (accretor, EX Hya systems). We therefore detail the comparison of models 2 and 4 of the accretion disc, which correspond to the respective accretor and propeller states.

Figure 14 demonstrates the density and velocity distributions in the equatorial plane (xy, upper plots) and the vertical plane (xz, bottom plots) for model 2 and model 4 near the time of the steady-state flow (about 17 orbital periods). In model 2, corresponding to the accretor state, the flow structure is similar to that in the case of synchronous rotation (see Fig. 6). The effect of the accretor spin leads to the formation of a larger tail of matter outflow through the Lagrange point L_3.

But the flow structure in model 4 is qualitatively different. The accretion disc has a larger size. The stream line from the inner Lagrange point L_1 even extends beyond the Roche lobe at some place. A powerful tail of matter overflowing through the outer Lagrange point L_3 into the external envelope is clearly visible. In the inner parts of the disc, a magnetospheric cavern is formed with the radius $(0.05-0.1)A$. The Kelvin–Helmholtz instability develops at the boundary of this cavern, leading to the formation of spiral waves, which tend to transform into shocks. As is evident from vertical cross sections of the flow (the bottom right panel), the matter from the envelope accretes mainly onto the disc, not onto the white dwarf.

Because there is almost no matter inside the cavern, the accretion rate onto the white dwarf in model 4 is close to zero.

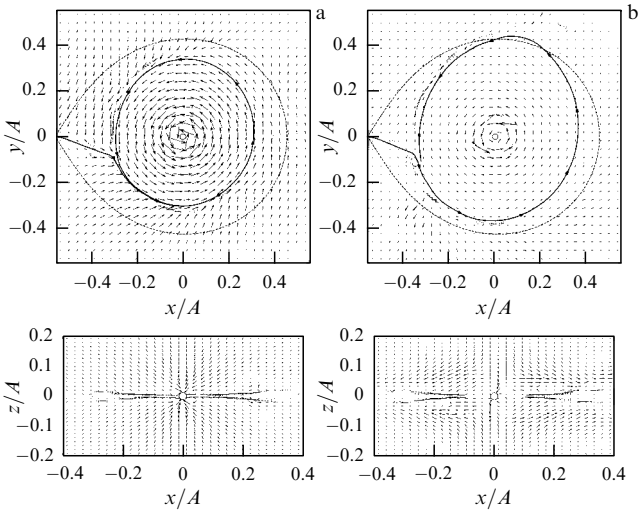

Figure 14. The density and velocity distributions in the equatorial (xy, top) and vertical (xz, bottom) planes in (a) model 2 (accretor) and (b) model 4 (propeller). The notation is the same as in Fig. 4.

On the other hand, the mass exchange process continues to supply matter to the disc, and hence its mass gradually increases.[2] By a certain time, the density at the cavern boundary can increase, such that matter penetrates the magnetosphere and starts accreting onto the white dwarf. After the excess mass has accreted, the system again transits to the propeller state. The described mechanism possibly explains quasiperiodic dwarf nova outbursts observed in DQ Her-type systems [5]. We note that the value of $P_{\rm spin}$ (see Section 4.1) in SS Cyg suggests that it belongs to the intermediate-polar type. Remarkably, SS Cyg demonstrates outbursts approximately every 200 orbital periods. The amplitude of the outbursts can be as high as 4.5^m. Assuming an accretion origin of the outbursts, such an increase in the luminosity of the system corresponds to the increase in the accretion rate by about 60 times. The flow structure in SS Cyg during the outburst was studied in [90] using the observed spectra and Doppler tomography.

Figure 15 shows the density and velocity distribution in the binary equatorial plane for model 5, which corresponds to AE Aqr type intermediate polars. In this case of a super-propeller, the accretor spin period $P_{\rm spin}$ was assumed to be 1000 times smaller than the orbital period $P_{\rm orb}$. The fast spin of the accretor prevents the formation of an accretion disc. Matter flowing from the donor through the Lagrange point L_1 is kept by the rapidly rotating magnetosphere of the white dwarf, gains additional momentum, and is expelled beyond the Roche lobe. A long tail winding around the binary system and forming its common envelope then appears. Figure 15 clearly shows that the Kelvin–Helmholtz instability develops along the tail. In addition to the main tail, several weaker parallel tails can be seen. Interestingly, some of them are connected by bars. The flow structure obtained in our calculations for model 5 is in good agreement with previous quasiparticle hydrodynamic calculations [22, 24]. We also note that the analysis of the observed Doppler tomograms of AE Aqr [22, 24] reveals similar structures in the matter flow in this system.

[2] Such accretion discs are frequently called storage discs (see, e.g., [8]).

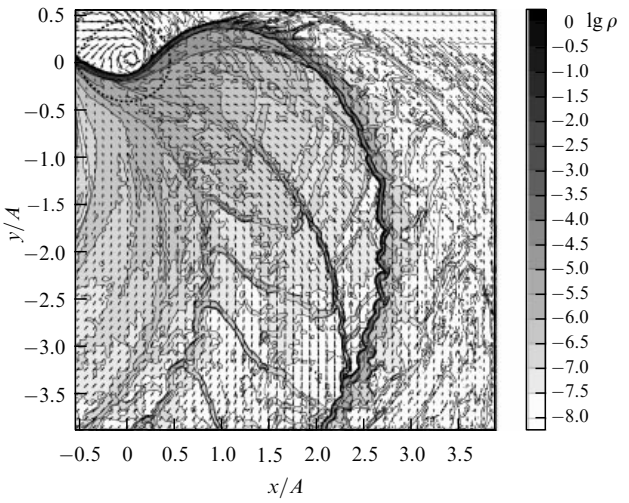

Figure 15. The density and velocity distributions in the equatorial plane in model 5 (superpropeller).

5. The magnetic field in an accretion disc

5.1 Mechanisms of field amplification

The magnetic field of a compact star can be amplified in the accretion disc due to differential rotation, radial motions, and the dynamo. The magnetic field can be reduced by diffusion, turbulent dissipation, and buoyancy.

In the inner parts of the disc, the generation of a toroidal magnetic field by differential rotation dominates [9]. The character of the generated field is determined by the rotation law in the disc. However, effects related to the poloidal velocity in the disc and redistributing the magnetic field across the disc can be significant here [49, 91–93]. The magnetic field can interact with waves emerging in the inner parts of the disc [18, 19] and lead to quasiperiodic variations of the accretion rate onto the compact star [31].

In the outer parts of the disc, the magnetic field can be partially amplified by the dynamo mechanism. In accretion discs in CBSs, both laminar (due to nonaxially symmetric flows) [94] and turbulent $\alpha\omega$-dynamos [38, 95, 96] can operate. The dynamo generation of the magnetic field in accretion discs was studied, e.g., in [9, 97–101]. For the dynamo generation of the magnetic field to be effective, the mean helicity α of nonaxially symmetric and turbulent gas motions must have no mirror symmetry relative to the disc equator. From the physical standpoint, this means that the number of right-screwed vortexes should not be equal to the number of left-screwed vortexes, because the Coriolis force produces an additional screwing of vortexes. When $\alpha > 0$, the quadrupole mode of the magnetic field dominates above the equatorial plane of the disc [39]. However, a detailed numerical modeling of magnetic turbulence [102, 103] due to the magneto-rotational instability [14, 15] in accretion discs showed that the opposite situation can be realized under certain conditions [104, 105]. In that case, the dipole magnetic field becomes dominant. We note that this component is favorable for the formation of bipolar outflows from the disc due to the centrifugal mechanism [13].

5.2 Results of numerical calculations

We consider the magnetic field behavior in the disc of a typical intermediate polar (model A in Section 4.3, model 1 in

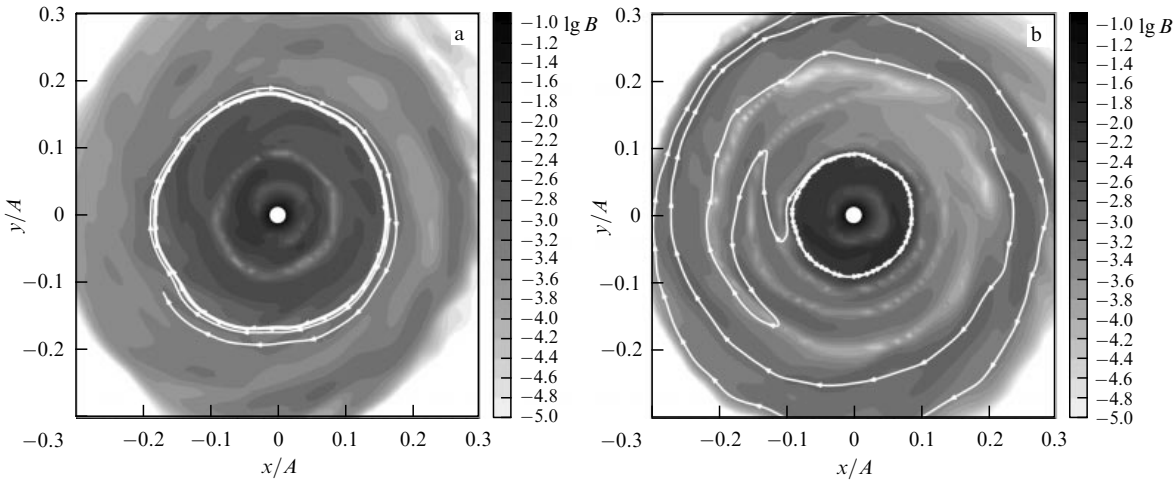

Figure 16. Magnetic field distribution in the equatorial plane of the disc near the times (a) $12.75P_{\rm orb}$ and (b) $13.36P_{\rm orb}$. The light line with arrows shows the magnetic field line passing through the point $x = -0.175A$, $y = 0.00A$.

Section 4.4). Figure 16 shows the distribution of the magnetic field B [in units $\sqrt{4\pi\rho(L_1)}A\Omega$] in the equatorial plane (xy) of the disc approaching the times $12.75P_{\rm orb}$ (Fig. 16a) and $13.36P_{\rm orb}$ (Fig. 16b). The light line with arrows shows the magnetic field line passing through the point $x = -0.175A$, $y = 0.00A$. The analysis of this figure suggests that there are three distinct zones in the disc: the inner zone of the intensive toroidal field generation due to differential rotation, the zone of current sheets, and the outer zone of the magnetic field dissipation. The inner zone radius is about $0.1A$. The current sheets in Fig. 16 show up as light rings. When passing through the current sheets, the magnetic field line changes to the opposite direction. In Fig. 16b, we can see at least three current sheets. The current-sheet zone extends from approximately $0.1A$ to $0.2A$. In Fig. 7, current sheets are located at the points where the toroidal field B_φ vanishes. In the far zone beyond $0.2A$, no intensive field generation due to differential rotation occurs, because the magnetic field of the compact star is very weak in this region. However, Fig. 7 indicates that a weak poloidal field is generated there. Therefore, the magnetic field in the accretion disc is predominantly toroidal.

A current sheet is formed at the boundary of the inner zone, or even inside it. The change of the sign of B_φ is related to a change of the rotation law in the disc. Near the central star, a transition zone is formed in which the angular momentum is strongly transported away. In this zone, the angular velocity of gas decreases from the Keplerian value to that of the field line rotation. The change in the rotation law affects the toroidal field generation.

These considerations can be illustrated with the following simple picture. We consider a model dependence of the angular velocity ω on the radius r,

$$\omega = \frac{\omega_0 (r/r_0)^a}{1 + (r/r_0)^{a+3/2}}\,, \tag{36}$$

where r_0 is some characteristic radius approximately equal to the magnetosphere radius. At $r \ll r_0$, we obtain the asymptotic dependence $\omega = \omega_0 (r/r_0)^a$ determining the rotation inside the magnetosphere. In the opposite limit $r \gg r_0$, expression (36) leads to the Keplerian rotation law $\omega = \omega_0 (r/r_0)^{-3/2}$. In Fig. 17, the magnetic field evolution and current sheet formation are shown. Figure 17a demonstrates the projection of the initial magnetic field lines on the equatorial plane. Figure 17b–d shows the picture of magnetic field lines evolving with rotation law (36) at times $2\pi/\omega_0$ (Fig. 17b), $4\pi/\omega_0$ (Fig. 17c), and $10\pi/\omega_0$ (Fig. 17d). The figure demonstrates that the current sheet and the magnetic zones can already be formed after the first several rotations of the disc. However, further evolution of these structures can be significantly affected by the magnetic field dissipation, radial motions, and the dynamo effect.

The above considerations suggest that in the case of equilibrium star rotation [8], when the corotation radius (the distance where the rotation velocity of the field lines matches that of the disc matter) is equal to the magnetosphere radius, the current sheet should not be formed. However, for this to be possible, the compact star should be significantly spun up

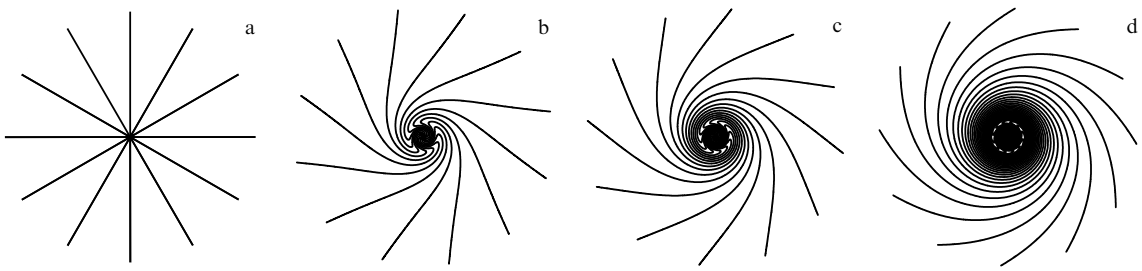

Figure 17. The formation of magnetic zones and current sheets in accretion discs. Shown is the schematic picture of magnetic field lines in the equatorial plane (a) at the beginning and after (b) one, (c) two, and (d) five disc rotations.

by the disc matter. In systems where the corotation radius exceeds that of the magnetosphere, current sheets must be formed. This condition is connected with the relation between the spin and magnetic field of accretor and the accretion rate. In our calculations, the rotation of the accretor was assumed to be synchronous. Hence, this condition is certainly satisfied. We note that in galaxies, the large-scale magnetic field generation by the dynamo mechanism in combination with a complex rotation law can also lead to the formation of magnetic zones and their separation into current sheets [39]. For example, the radius of the current ring in galaxy M31 is about 3 kpc.

The current sheet formed is carried away into the outer parts of the disc due to the decretion of matter [32]. It is replaced by a new current sheet formed after some time. Thus, several current sheets can be simultaneously present in the disc. The alternating occurrence of accretion and decretion modes in the inner parts of the disc can be explained by the quasiperiodic character of magnetic field generation. Indeed, the field generation must increase the radial pressure gradient of the toroidal magnetic field, which ultimately stops accretion. The transition of the inner parts of the disc to the decretion regime appears as minima of the accretion rate (see Fig. 9). Once the field is transported into the outer regions of the disc, the magnetic pressure decreases and the accretion regime resumes. The field distribution variations in the inner zone can also be seen in Fig. 16.

An enhanced magnetic field dissipation occurs in current sheets, leading to an increase in temperature and UV or X-ray luminosity. In addition, because of the magnetic field decrease in the current sheet, the total pressure also decreases. Hence, the disc thickness must also decrease in the current sheet region. This conclusion is supported by numerical calculations.

5.3 Main features of field generation in discs

The flow in an accretion disc is turbulent, and hence the velocity and the magnetic field can be represented as the sum of the mean values and low-scale fluctuations. To explore the main features of the magnetic field generation in accretion discs, we consider a simplified model in which the dipole magnetic field axis coincides with the spin axis of the star. In this case, we can use the axially symmetric approximation to describe the magnetic field averaged over turbulent pulsations and the azimuth [30].

The induction equation for averaged values with the dynamo effect taken into account can be written in the form

$$\frac{\partial \mathbf{b}}{\partial t} = \operatorname{rot}\left(\mathbf{v}\times\mathbf{B}_* + \mathbf{v}\times\mathbf{b} + \alpha\mathbf{b} - \eta\operatorname{rot}\mathbf{b}\right), \tag{37}$$

where α is an axially symmetric function related to the helicity of the flow [see (10)]. Equation (37) implies that the turbulent character of the flow in an accretion disc leads not only to the field winding by differential rotation but also to the poloidal magnetic field generation ($\alpha\omega$-dynamo). In our model, the turbulent viscosity is not explicitly taken into account. However, numerical viscosity is always present, which is determined by the finite-difference system used and the grid resolution. The results of numerical modeling allow determining the value of the Shakura–Sunyaev α_{T} parameter [50] characterizing the turbulent viscosity in accretion discs.

In accretion discs in binary systems, the orbits of particles are elliptical, and therefore the flow is not axially symmetric. This may lead to an additional dynamo effect. Averaging the induction equation over the azimuth also leads to Eqn (37), in which the mean values are assumed to be averaged axially symmetric quantities, and fluctuations describe deviations that are not axially symmetric. In the case where axially nonsymmetric terms are small compared with axially symmetric ones and the magnetic field is almost toroidal, the induction equation can be shown to also have form (37) [94].

The magnetic field of a compact star is poloidal ($\mathbf{B}_{*\varphi} = 0$, $\mathbf{B}_{*\mathrm{p}} = \mathbf{B}_*$), and therefore the toroidal component of the field is $\mathbf{b}_\varphi = \mathbf{B}_\varphi$. We set $\mathbf{b}_\mathrm{p} = \operatorname{rot}(A\mathbf{n}_\varphi)$, where $\mathbf{n}_\varphi$ is a unit azimuthal vector. With this notation, Eqn (37) can be rewritten in the form of the system of equations

$$\frac{\partial A}{\partial t} + \frac{1}{r}(\mathbf{v}_\mathrm{p}\nabla)(rA) = \alpha B_\varphi + \eta\left(\nabla^2 A - \frac{A}{r^2}\right), \tag{38}$$

$$\frac{\partial B_\varphi}{\partial t} = r(\mathbf{B}_\mathrm{p}\nabla)\omega - r\nabla\left(\frac{B_\varphi}{r}\,\mathbf{v}_\mathrm{p}\right) - \frac{1}{r}\,\nabla\alpha\,\nabla(rA) - \alpha\left(\nabla^2 A - \frac{A}{r^2}\right) + \eta\left(\nabla^2 B_\varphi - \frac{B_\varphi}{r^2}\right), \tag{39}$$

where $\omega = v_\varphi/r$ is the angular rotation velocity in the disc.

In an accretion disc, these equations can be significantly simplified. Because $|v_r|, |v_z| \ll |v_\varphi|$ in an accretion disc, we can set $\mathbf{v}_\mathrm{p} = 0$. Moreover, it is possible to neglect the insignificant third and fourth terms in the right-hand side of Eqn (39), which are responsible for the α^2-dynamo. In diffusion terms, radial derivatives can be neglected in comparison to vertical ones because their ratio is of the order of $z/r \ll 1$. Further, using the estimates $\partial\omega/\partial z \approx z/r\,\partial\omega/\partial r$, $|b_z\,\partial\omega/\partial z| \ll |b_r\,\partial\omega/\partial r|$, and

$$B_{*r} = \frac{3}{2}\,B_\mathrm{a}\left(\frac{R_\mathrm{a}}{r}\right)^3\frac{z}{r}, \qquad B_{*z} = -\frac{1}{2}\,B_\mathrm{a}\left(\frac{R_\mathrm{a}}{r}\right)^3, \tag{40}$$

we find

$$r(\mathbf{B}_\mathrm{p}\nabla)\omega = \frac{z}{r}\,gB_0 - g\,\frac{\partial A}{\partial z}, \tag{41}$$

where B_a is the magnetic field on the surface of the star, $g = r\,\partial\omega/\partial r$ is the measure of the differential rotation, and $B_0 = B_\mathrm{a}(R_\mathrm{a}/r)^3$ is the characteristic magnetic field in the disc. Finally, we assume that g and η depend only on r.

After these simplifications, we arrive at the system of equations

$$\frac{\partial A}{\partial t} = \alpha B_\varphi + \eta\,\frac{\partial^2 A}{\partial z^2}, \tag{42}$$

$$\frac{\partial B_\varphi}{\partial t} = \frac{z}{r}\,gB_0 - g\,\frac{\partial A}{\partial z} + \eta\,\frac{\partial^2 B_\varphi}{\partial z^2}. \tag{43}$$

These equations have a simple physical interpretation. Equation (42) describes the evolution of the poloidal magnetic field in the disc. The first term in the right-hand side describes the generation of the poloidal field from the toroidal one by the dynamo effect, and the second term determines the poloidal magnetic field dissipation. Equation (43) describes the evolution of the toroidal magnetic field in the disc. The first and the second terms in the right-hand side determine the generation of the toroidal field from the magnetic field of the star and the poloidal field generated by differential rotation in the disc. The last term in the right-hand side describes the toroidal magnetic field dissipation.

In the inner parts of the disc, the dynamo effect is weak and the magnetic field is amplified due to differential rotation. In that case, the term αB_φ can be neglected in Eqn (42). As a result, $A = 0$, and hence only the toroidal magnetic field is generated. The remaining equation (43) then takes the form

$$\frac{\partial B_\varphi}{\partial t} = \frac{z}{r}\, g B_0 + \eta\, \frac{\partial^2 B_\varphi}{\partial z^2}\,. \tag{44}$$

The general solution of Eqn (44) satisfying the initial condition $B_\varphi(t=0)=0$ and boundary conditions $B_\varphi(z=0)=B_\varphi(z=H)=0$ can be written as

$$B_\varphi = 2B_{\varphi,0} \sum_{n=1}^{\infty} \frac{(-1)^n}{(\pi n)^3} \left\{ 1 - \exp\left[-(\pi n)^2\, \frac{t}{t_\mathrm{d}} \right] \right\} \sin\frac{\pi n z}{H}\,, \tag{45}$$

where $B_{\varphi,0} = g B_0 H t_\mathrm{d}/r$ and $t_\mathrm{d} = H^2/\eta$ is the diffusion time. At early stages of generation at $t \ll t_\mathrm{d}$, the toroidal field increases linearly with time, $B_\varphi = g B_0 z t/r$. This solution also describes field generation in the ideal MHD case with $\eta = 0$. However, we note that this leads to a discontinuity of B_φ on the disc surface at $z = H$. This means that dissipative processes should play a significant role near the disc surface, and they cannot therefore be neglected, at least in this region. In the other limit case, at $t \gg t_\mathrm{d}$, we obtain a stationary solution

$$B_\varphi = \frac{1}{6}\, B_{\varphi,0}\, \frac{z}{H} \left(1 - \frac{z^2}{H^2} \right). \tag{46}$$

The maximum absolute value of the magnetic field B_φ is reached at $z = H/\sqrt{3}$. The mean magnetic field over the disc height is $\bar{B}_\varphi = B_{\varphi,0}/24$.

The factor $B_{\varphi,0}$ in (46) describes the radial structure of the toroidal field. We consider model dependence (36) of the angular rotation velocity in the disc. Assuming that $H \propto r$ and $\eta \propto r$, we can obtain the asymptotic laws $B_{\varphi,0} \propto r^{a-2}$ at $r \ll r_0$ and $B_{\varphi,0} \propto r^{-7/2}$ at $r \gg r_0$. The behavior of $B_{\varphi,0}$ as $r \to 0$ essentially depends on the parameter a characterizing the rotation of the disc in the accretor magnetosphere: $B_{\varphi,0} \to \infty$ for $a < 2$, $B_{\varphi,0} \to \mathrm{const}$ for $a = 2$, and $B_{\varphi,0} \to 0$ for $a > 2$. At the point $r = (2a/3)^{1/(a+3/2)} r_0$, the sign of the magnetic field reverses. This means that at this radius, the neighboring magnetic lines are directed oppositely, which leads to the formation of a current sheet separating two magnetic rings. The magnetic fields in the inner and outer magnetic ring have opposite direction. We recall that numerical modeling supports this picture (see Fig. 7).

The asymptotic character of the dependence of B_φ on z is related to the assumption that the magnetic axis of the star coincides with the spin axis. If the magnetic field is tilted, the antisymmetry of the field relative to the equatorial plane is violated. This situation is illustrated in Fig. 18. For a tilted magnetic field, a vertical magnetic field gradient appears in the disc (shown by white arrows). On the right side of the figure, the field increases from bottom up, and on the left side, from top down. As a result, the stronger field is increased first. In view of the direction of rotation in the disc, the field directed outward from (toward) the reader on the right (left) side of the figure increases faster. In both cases, the resulting toroidal field is positive. The same distribution of the toroidal field is obtained in numerical calculations. The effect is strongest for the field tilt angle

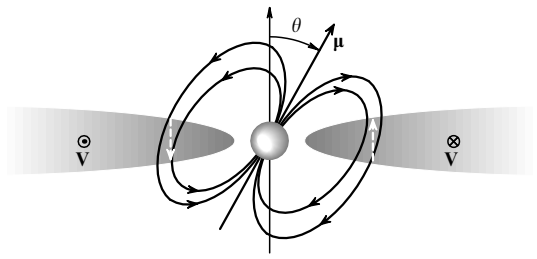

Figure 18. Explanation of the generation of the quadrupole component of the toroidal magnetic field in the accretion disc around a tilted magnetic field.

$\theta = 45°$. These considerations lead to the following conclusion. The antisymmetric toroidal field (the dipole model) is generated only at $\theta = 0°$ and $90°$. Any small deviations from these values suppress the dipole mode by the quadrupole one. Hence, the generation of a purely dipole mode in accretion discs of intermediate polars can be unstable. The quadrupole mode is more stable. We also recall that the dynamo mechanism in the outer parts of the disc amplifies the quadrupole magnetic field component first [39].

In the outer parts of the disc, the dynamo effect can play a significant role in magnetic field generation. Therefore, to describe the magnetic field, we should use the complete system of equations (42), (43). The value of α in these equations is determined by the mean helicity of the velocity fluctuations $\delta\mathbf{v}$,

$$\alpha = -\frac{\tau}{3}\, \langle \delta\mathbf{v}\, \mathrm{rot}\, \delta\mathbf{v} \rangle\,, \tag{47}$$

where τ is the characteristic correlation time. The angular brackets denote ensemble averaging over turbulent pulsations and azimuthal motion. In both cases, the characteristic correlation time can be estimated as $\tau = H/(\alpha_\mathrm{T} c_\mathrm{s})$.

Figure 19 shows the vertical distribution of α for nonazimuthal velocity fluctuations in an accretion disc at different distances from the accretor obtained in 3D MHD modeling. The figure shows that the helicity has mirror antisymmetry relative to the disc plane, which is a necessary condition for the dynamo mechanism to be effective [39]. Apparently, similar profiles are obtained for turbulent velocity fluctuations. To simplify the analysis in what

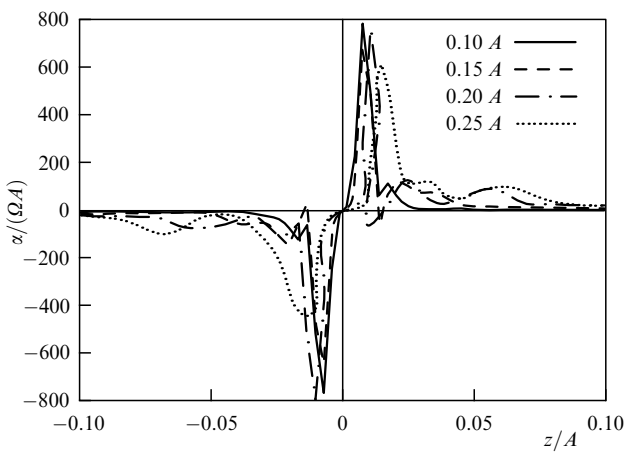

Figure 19. The mean helicity α distribution in the accretion disc at different distances from the accretor.

follows, we use the values of α averaged over the disc half-thickness.

We restrict ourselves to stationary solutions of Eqns (42) and (43). In this case, the equations can be reduced to a single equation for the toroidal field:

$$\frac{\partial^3 B_\varphi}{\partial z^3} + \frac{\alpha g}{\eta^2} B_\varphi + \frac{g B_0}{\eta r} = 0 . \tag{48}$$

This equation is invariant under the transformations $z \to -z$ with the simultaneous change of the function $B_\varphi(z) \to -B_\varphi(-z)$. This means that it describes the generation of the dipole (antisymmetric) component of the magnetic field, with $B_\varphi(-z) = -B_\varphi(z)$. As was shown in the preceding section, such a field is generated from the magnetic field of the accreting star by differential rotation of the disc. However, at far distances from the accretor, where $gB_0H^3/\eta r \ll 1$, the quadrupole (symmetric) field component, $B_\varphi(-z) = B_\varphi(z)$, can become dominant [39].

Due to the linearity of Eqn (48), its general solution can be represented in the form $B_\varphi = B_\varphi^{(\mathrm{d})} + B_\varphi^{(\mathrm{q})}$. The components $B_\varphi^{(\mathrm{d})}$ and $B_\varphi^{(\mathrm{q})}$ describe the dipole and quadrupole fields, and satisfy the equations

$$\frac{\partial^3 B_\varphi^{(\mathrm{d})}}{\partial z^3} + \frac{\alpha g}{\eta^2} B_\varphi^{(\mathrm{d})} + \frac{g B_0}{\eta r} = 0 , \tag{49}$$

$$\frac{\partial^3 B_\varphi^{(\mathrm{q})}}{\partial z^3} + \frac{\alpha g}{\eta^2} B_\varphi^{(\mathrm{q})} = 0 . \tag{50}$$

These equations can be conveniently rewritten in a dimensionless form. We set $B_\varphi^{(\mathrm{d,q})} = B_{\varphi,0} f_{\mathrm{d,q}}(\zeta)$, where $\zeta = z/H$. Then Eqns (49) and (50) become

$$f_\mathrm{d}''' + D f_\mathrm{d} + 1 = 0 , \tag{51}$$

$$f_\mathrm{q}''' + D f_\mathrm{q} = 0 , \tag{52}$$

where $D = \alpha g H^3/\eta^2$ is the dynamo number and primes denote derivatives with respect to ζ. These equations must be solved with the boundary conditions $f_\mathrm{d}(0) = f_\mathrm{d}(1) = 0$, $f_\mathrm{d}''(1) = -1$, and $f_\mathrm{q}'(0) = f_\mathrm{q}(1) = f_\mathrm{q}''(1) = 0$. In addition, we note that in the outer parts of the disc, at $z > 0$, the dynamo number D must be negative, because the measure of the differential rotation is negative there.

The solution of these equations determines the vertical field structure [32]. It is interesting to note that with the dynamo effect taken into account, the radial field structure is again described by the factor $B_{\varphi,0}$. In the inner magnetic ring, for a tilted magnetic axis, the quadrupole field component is always dominant. In the outer magnetic ring, the quadrupole field component can also become dominant with time because it grows faster than the dipole component due to the dynamo effect [39]. This structure of the magnetic field in the outer and the inner magnetic rings is confirmed by 3D numerical calculations.

6. Conclusion

The main results of the review can be formulated as follows.

(1) A 3D numerical model is developed to study mass exchange in CBSs taking the magnetic field of the accreting star into account. The mathematical model assumes that the proper magnetic field of the accreting star is potential and consists of dipole and quadrupole components. The magnetic axis tilt relative to the spin axis, magnetic field diffusion, and radiative heating and cooling are also taken into account.

(2) It is established that in models with a relatively low magnetic field $B_\mathrm{a} \leqslant 10^6$ G, an accretion disc is formed. The disc shows the characteristic features, including a 'hot line', tidal shocks, and a precessing spiral density wave. The radius of the calculated magnetosphere is in good agreement with estimates of the inner accretion disc radius in SS Cyg inferred from the analysis of observed Doppler tomograms. With increasing B_a, the accretion disc size decreases and the magnetosphere radius increases. These models correspond to flows in intermediate polars.

In models with strong magnetic fields $B_\mathrm{a} > 10^6$ G, an accretion disc is not formed. The flow has the form of an accretion stream that starts from the inner Lagrange point L_1 and ends on the magnetic poles of the accretor. These models corresponds to flows in polars.

The magnetic field $B_\mathrm{a} = 10^6$ G separating the two types of flows is determined by the relation between the minimum distance by which the stream approaches the accretor R_min and the magnetosphere radius r_m. An accretion disc is formed if $R_\mathrm{min} > r_\mathrm{m}$. Otherwise, the accretion flow is inside the region of the significant influence of the magnetic field of the accretor and no accretion disc is formed. This estimate of the magnetic field separating polars and intermediate polars is very general and depends weakly on parameters of the specific binary system.

(3) It is shown that the presence of a strong quadrupole magnetic field component significantly complicates the character of accretion in comparison with the case of a purely dipole field. In particular, the formation of additional accretion zones near the magnetic belt, which is located somewhat below the magnetic equator of the accretor, is discovered. In this picture, radiation from hot spots near magnetic poles is significantly polarized, because the magnetic field has a distinct direction there, while radiation from spots formed near the magnetic belt is not polarized. The analysis of CBSs with a complex magnetic field (for example, BY Cam) confirms the results of our modeling.

(4) Asynchronous rotation of the accreting star has a strong effect on the flow structure in magnetic CBSs. In the case of slow rotation ($P_\mathrm{spin} > 0.033 P_\mathrm{orb}$, the 'accretor' state), the flow structure is similar to that obtained for synchronous rotation.

In the case of fast rotation ($P_\mathrm{spin} < 0.033 P_\mathrm{orb}$, the 'propeller' state), a magnetospheric cavern is formed near the accretor and the accretion rate almost vanishes. The gradual growth of the disc mass ultimately leads to the suppression of the cavern, the fall of the stored mass onto the surface of the accretor, and a drastic increase in the mass accretion rate. According to our numerical calculations, this mechanism of mass accretion rate variations can be used to explain quasiperiodic outbursts in dwarf novae observed in DQ Her systems.

In the case of very fast rotation ($P_\mathrm{spin} < 0.033 P_\mathrm{orb}$), no accretion disc is formed. Matter is expelled from the magnetosphere and forms a spiral tail winding around the binary system. These flows are observed in AE Aqr systems.

(5) The analysis of magnetic field generation in accretion discs of CBSs revealed that the field in the disc is predominantly toroidal. Three zones can be distinguished in the disc: the inner zone of intensive magnetic field generation due to differential rotation, the zone of current sheets, and the outer zone of magnetic field dissipation. The magnetic field

amplification in the inner parts of the disc is shown to lead to a very strong increase in the corresponding pressure gradient, which stops accretion. The drift of the field into the outer parts of the disc decreases the magnetic pressure and helps resume accretion. The alternation of accretion and decretion states in the inner parts of the disc caused by the quasiperiodic character of magnetic field generation is thus discovered. This effect leads to a significant change (15–25%) in the accretion rate onto the compact star and should be observed as brightness variability of the system.

Yet another consequence of the quasiperiodic character of the magnetic field amplification is the simultaneous presence of several current sheets in the disc. The current sheet formed near the magnetosphere of the accretor is brought away to the outer parts of the disc by decretion and another current sheet is formed in its place after some time. Current sheets can be formed only in systems in which the corotation radius exceeds that of the magnetosphere (the accretor state). This condition depends on the relation between the spin period of the accretor, its magnetic field, and the mass accretion rate. Clearly, changes in the disc parameters and additional radiation caused by the formation of current sheets should be taken into account when interpreting observations of CBSs in classical astronomy.

The work was supported by the Russian Academy of Sciences, the Russian Foundation for Basic Research (projects 09-02-00064 and 11-02-00076), the Federal Agency of Science and Innovations, and the Special Federal Program "Scientific and teaching Researchers of Innovative Russia for 2009–2013."

References

1. Masevich A G, Tutukov A V *Evolyutsiya Zvezd: Teoriya i Nablyudeniya* (Evolution of Stars: Theory and Observations) (Moscow: Nauka, 1988)
2. Paczyński B, Sienkiewicz R *Acta Astron.* **22** 73 (1972)
3. Lubow S H, Shu F H *Astrophys. J.* **198** 383 (1975)
4. Boyarchuk A A et al. *Mass Transfer in Close Binary Stars* (London: Taylor & Francis, 2002)
5. Warner B *Cataclysmic Variable Stars* (Cambridge: Cambridge Univ. Press, 2003)
6. Fridman A M, Bisikalo D V *Usp. Fiz. Nauk* **178** 577 (2008) [*Phys. Usp.* **51** 551 (2008)]
7. Norton A J, Wynn G A, Somerscales R V *Astrophys. J.* **614** 349 (2004)
8. Lipunov V M *Astrofizika Neitronnykh Zvezd* (Astrophysics of Neutron Stars) (Moscow: Nauka, 1987) [Translated into English (Heidelberg: Springer, 1992)]
9. Campbell C G *Magnetohydrodynamics in Binary Stars* (Dordrecht: Kluwer Acad. Publ., 1997)
10. Dolginov A Z *Usp. Fiz. Nauk* **152** 231 (1987) [*Sov. Phys. Usp.* **30** 475 (1987)]
11. Herzenberg A *Philos. Trans. R. Soc. London A* **250** 543 (1958)
12. Brandenburg A, Moss D, Soward A M *Proc. R. Soc. London A* **454** 1283 (1998)
13. Blandford R D, Payne D G *Mon. Not. R. Astron. Soc.* **199** 883 (1982)
14. Velikhov E P *Zh. Eksp. Teor. Fiz.* **36** 1398 (1959) [*Sov. Phys. JETP* **9** 995 (1959)]
15. Balbus S A, Hawley J F *Rev. Mod. Phys.* **70** 1 (1998)
16. Bisikalo D V et al. *Astron. Zh.* **77** 31 (2000) [*Astron. Rep.* **44** 26 (2000)]
17. Bisikalo D V et al. *Astron. Zh.* **80** 879 (2003) [*Astron. Rep.* **47** 809 (2003)]
18. Bisikalo D V et al. *Astron. Zh.* **81** 494 (2004) [*Astron. Rep.* **48** 449 (2004)]
19. Bisikalo D V et al. *Astron. Zh.* **82** 788 (2005) [*Astron. Rep.* **49** 701 (2005)]
20. King A R *Mon. Not. R. Astron. Soc.* **261** 144 (1993)
21. Wynn G A, King A R *Mon. Not. R. Astron. Soc.* **275** 9 (1995)
22. Wynn G A, King A R, Horne K *Mon. Not. R. Astron. Soc.* **286** 436 (1997)
23. King A R, Wynn G A *Mon. Not. R. Astron. Soc.* **310** 203 (1999)
24. Ikhsanov N R, Neustroev V V, Beskrovnaya N G *Astron. Astrophys.* **421** 1131 (2004)
25. Norton A J et al. *Astrophys. J.* **672** 524 (2008)
26. Koldoba A V et al. *Astrophys. J.* **576** L53 (2002)
27. Romanova M M et al. *Astrophys. J.* **595** 1009 (2003)
28. Romanova M M et al. *Astrophys. J.* **610** 920 (2004)
29. Romanova M M et al. *Astrophys. J.* **616** L151 (2004)
30. Zhilkin A G, Bisikalo D V *Astron. Zh.* **86** 475 (2009) [*Astron. Rep.* **53** 436 (2009)]
31. Zhilkin A G, Bisikalo D V *Adv. Space Res.* **45** 437 (2010)
32. Zhilkin A G, Bisikalo D V *Astron. Zh.* **87** 913 (2010) [*Astron. Rep.* **54** 840 (2010)]
33. Zhilkin A G, Bisikalo D V *Astron. Zh.* **87** 1155 (2010) [*Astron. Rep.* **54** 1063 (2010)]
34. Piirola V et al. *Astron. Astrophys.* **283** 163 (1994)
35. Mason P A et al. *ASP Conf. Ser.* **85** 496 (1995)
36. Landau L D, Lifshitz E M *Teoriya Polya* (The Classical Theory of Fields) (Moscow: Fizmatlit, 2006) [Translated into English (Oxford: Pergamon Press, 1980)]
37. Landau L D, Lifshitz E M, Pitaevskii L P *Elektrodinamika Sploshnykh Sred* (Electrodynamics of Continuous Media) (Moscow: Fizmatlit, 2003) [Translated into English (Oxford: Pergamon Press, 1984)]
38. Parker E N *Cosmical Magnetic Fields: Their Origin and Their Activity* (Oxford: Clarendon Press, 1979) [Translated into Russian (Moscow: Mir, 1982)]
39. Ruzmaikin A A, Shukurov A M, Sokoloff D D *Magnitnye Polya Galaktik* (Magnetic Fields of Galaxies) (Moscow: Nauka, 1988) [Translated into English (Dordrecht: Kluwer Acad. Publ., 1988)]
40. Cox D P, Daltabuit E *Astrophys. J.* **167** 113 (1971)
41. Dalgarno A, McCray R A *Annu. Rev. Astron. Astrophys.* **10** 375 (1972)
42. Raymond J C, Cox D P, Smith B W *Astrophys. J.* **204** 290 (1976)
43. Spitzer L (Jr.) *Physical Processes in the Interstellar Medium* (New York: Wiley, 1978) [Translated into Russian (Moscow: Mir, 1981)]
44. Zhilkin A G *Mat. Modelirovanie* **22** (1) 110 (2010)
45. Frank-Kamenetskii D A *Lektsii po Fizike Plazmy* (Lectures in Plasma Physics) (Moscow: Atomizdat, 1968)
46. Chen F *Introduction to Plasma Physics* (New York: Springer, 1995) [Translated into Russian (Moscow: Mir, 1987)]
47. Trubnikov B A *Teoriya Plazmy* (Theory of Plasma) (Moscow: Energoatomizdat, 1996)
48. Drell S D, Foley H M, Ruderman M A *J. Geophys. Res.* **70** 3131 (1965)
49. Bisnovatyi-Kogan G S, Ruzmaikin A A *Astrophys. Space. Sci.* **42** 401 (1976)
50. Shakura N I *Astron. Zh.* **49** 921 (1972) [*Sov. Astron.* **16** 756 (1972)]
51. Lifshitz E M, Pitaevskii L P *Fizicheskaya Kinetika* (Physical Kinetics) (Moscow: Fizmatlit, 2007) [Translated into English (Oxford: Pergamon Press, 1981)]
52. Zhilkin A G *Zh. Vychisl. Mat. Mat. Fiz.* **47** 1898 (2007) [*Comput. Math. Math. Phys.* **47** 1819 (2007)]
53. Tanaka T *J. Comput. Phys.* **111** 381 (1994)
54. Powell K G et al. *J. Comput. Phys.* **154** 284 (1999)
55. Kulikovskii A G, Pogorelov N V, Semenov A Yu *Matematicheskie Voprosy Chislennogo Resheniya Giperbolicheskikh Sistem Uravnenii* (Mathematical Aspects of Numerical Solution of Hyperbolic Systems) (Moscow: Fizmatlit, 2001) [Translated into English (Boca Raton: Chapman and Hall/CRC, 2001)]
56. Dellar P J *J. Comput. Phys.* **172** 392 (2001)
57. Samarskii A A *Teoriya Raznostnykh Skhem* (The Theory of Difference Schemes) (Moscow: Nauka, 1989) [Translated into English (New York: Marcel Dekker, 2001)]
58. Zhilkin A G, Bisikalo D V, in *Materialy Dokladov X Mezhdunarod. Nauchnoi Konf. Zababakhinskie Nauchnye Chteniya, 15–19 Marta 2010, Snezhinsk, Chelyabinskaya Obl., Russiya* (Proc. of the X Intern. Conf. Zababakhin Scientific Readings, March 15–19, 2010, Snezhinsk, Chelyabinsk region, Russia); http://www.vniitf.ru/images/zst/2010/sec6/6-7.pdf

59. Paczyński B *Astrophys. J.* **216** 822 (1977)
60. Nagasawa M, Matsuda T, Kuwahara K *Numer. Astrophys. Jpn.* **2** 27 (1991)
61. Hirose M, Osaki Y, Mineshige S *Publ. Astron. Soc. Jpn.* **43** 809 (1991)
62. Molteni D, Belvedere G, Lanzafame G *Mon. Not. R. Astron. Soc.* **249** 748 (1991)
63. Bisikalo D V et al. *Astron. Zh.* **78** 707 (2001) [*Astron. Rep.* **45** 611 (2001)]
64. Molteni D et al. *Mon. Not. R. Astron. Soc.* **327** 1103 (2001)
65. Bisikalo D V et al. *Astron. Zh.* **81** 648 (2004) [*Astron. Rep.* **48** 588 (2004)]
66. Bisikalo D V *Astrophys. Space Sci.* **296** 391 (2005)
67. Bisikalo D V et al. *Chin. J. Astron. Astrophys.* **6** 159 (2006)
68. Khruzina T S et al. *Astron. Zh.* **78** 625 (2001) [*Astron. Rep.* **45** 538 (2001)]
69. Khruzina T S et al. *Astron. Zh.* **80** 675 (2003) [*Astron. Rep.* **47** 621 (2003)]
70. Khruzina T S et al. *Astron. Zh.* **80** 919 (2003) [*Astron. Rep.* **47** 848 (2003)]
71. Khruzina T S et al. *Astron. Zh.* **82** 99 (2005) [*Astron. Rep.* **49** 79 (2005)]
72. Lyubarskij Yu E, Postnov K A, Prokhorov M E *Mon. Not. R. Astron. Soc.* **266** 583 (1994)
73. Ogilvie G I *Mon. Not. R. Astron. Soc.* **325** 231 (2001)
74. Sytov A Yu et al. *Astron. Zh.* **84** 926 (2007) [*Astron. Rep.* **51** 836 (2007)]
75. Sytov A Yu et al. *Astron. Zh.* **86** 250 (2009) [*Astron. Rep.* **53** 223 (2009)]
76. Sytov A Yu et al. *Astron. Zh.* **86** 468 (2009) [*Astron. Rep.* **53** 428 (2009)]
77. Giovannelli F et al. *Acta Astron.* **33** 319 (1983)
78. Fabbiano G et al. *Astrophys. J.* **243** 911 (1981)
79. Kjurkchieva D, Marchev D, Ogloza W *Astrophys. Space Sci.* **262** 53 (1999)
80. Sion E M *Publ. Astron. Soc. Pacif.* **111** 532 (1999)
81. Martinez-Pais I G et al. *Astron. Astrophys.* **291** 455 (1994)
82. Sawada K, Matsuda T, Hachisu I *Mon. Not. R. Astron. Soc.* **219** 75 (1986)
83. Tayler R J *Mon. Not. R. Astron. Soc.* **161** 365 (1973)
84. Ardeljan N V, Bisnovatyi-Kogan G S, Moiseenko S G *Mon. Not. R. Astron. Soc.* **359** 333 (2005)
85. Spruit H C *Astron. Astrophys.* **381** 923 (2002)
86. Bisikalo D V et al. *Astron. Zh.* **85** 356 (2008) [*Astron. Rep.* **52** 318 (2008)]
87. Giovannelli F, Sabau-Graziati L *Mem. Soc. Astron. It.* **70** 987 (1999)
88. Romanova M M et al. *Astrophys. J.* **635** L165 (2005)
89. Ustyugova G V et al. *Astrophys. J.* **646** 304 (2006)
90. Kononov D A et al. *Astron. Zh.* **85** 927 (2008) [*Astron. Rep.* **52** 835 (2008)]
91. Bisnovatyi-Kogan G S, Ruzmaikin A A *Astrophys. Space Sci.* **28** 45 (1974)
92. Bisnovatyi-Kogan G S, Lovelace R V E *Astrophys. J.* **667** L167 (2007)
93. Rothstein D M, Lovelace R V E *Astrophys. J.* **677** 1221 (2008)
94. Braginskii S I *Zh. Eksp. Teor. Fiz.* **47** 2178 (1964) [*Sov. Phys. JETP* **20** 1462 (1964)]
95. Moffatt H K *Magnetic Field Generation in Electrically Conducting Fluids* (Cambridge: Cambridge Univ. Press, 1978)
96. Vainshtein S I, Zel'dovich Ya B, Ruzmaikin A A *Turbulentnoe Dinamo v Astrofizike* (Turbulent Dynamo in Astrophysics) (Moscow: Nauka, 1980)
97. Parker E N *Astrophys. J.* **163** 255 (1971)
98. Pudritz R E *Mon. Not. R. Astron. Soc.* **195** 897 (1981)
99. Stepinski T F, Levy E H *Astrophys. J.* **362** 318 (1990)
100. Rudiger G, Elstner D, Stepinski T F *Astron. Astrophys.* **298** 934 (1995)
101. Campbell C G *Mon. Not. R. Astron. Soc.* **361** 396 (2005)
102. Brandenburg A et al. *Astrophys. J.* **446** 741 (1995)
103. Ziegler U, Rudiger G *Astron. Astrophys.* **356** 1141 (2000)
104. Brandenburg A, Sokoloff D *Geophys. Astrophys. Fluid Dyn.* **96** 319 (2002)
105. von Rekowski B et al. *Astron. Astrophys.* **398** 825 (2003)